Regulation of the collagen IV network by the basement membrane protein perlecan is crucial for squamous epithelial cell morphogenesis and organ architecture

Raphaël Bonche, Prune Smolen, Aline Chessel, Séverine Boisivon, Sabrina Pisano, Aaron Voigt, Sébastien Schaub, Pascal Thérond, Sandrine Pizette

Regulation of squamous epithelial cell morphogenesis by the basement membrane protein Perlecan is crucial for organ architecture

Raphaël Bonche[1*], Aline Chessel[1*], Séverine Boisivon[1], Aaron Voigt[2], Sébastien Schaub[1], Pascal Thérond[1§] and Sandrine Pizette[1,3§]

[1]Université Côte d'Azur, CNRS, Inserm, Institut de Biologie Valrose, Nice 06108, France

[2]Department of Neurology, University Medical Center, RWTH Aachen University, Aachen, 52074, Germany

[3]Corresponding author (email: pizette@unice.fr)

*joint first authors

[§]joint senior authors

ABSTRACT

All epithelia are surrounded by a specialized extracellular matrix, the basement membrane (BM). During development, this BM contributes to the morphogenesis of epithelial organs through different functions, the most recently added one being the shaping of the tissue. Seminal studies highlight the importance of the mechanical properties of the BM in this process. These rely on two of its core components, Collagen type IV and Perlecan, the first one supplying the BM with rigidity to constrain the tissue, the second one antagonizing this effect. Nevertheless, the number of organs that has been inspected is still scarce, and given that epithelial tissues exhibit a wide array of shapes, their forms are bound to be regulated by distinct mechanisms. This is underscored by mounting evidence that BM composition and assembly/biogenesis is tissue-specific. Moreover, previous reports have essentially focused on the mechanical role of the BM in morphogenesis at the tissue scale, but not the cell scale. Here, we took advantage of the robust conservation of core BM proteins and the limited genetic redundancy of the *Drosophila* model system to address how this matrix shapes a complex organ comprising a squamous, a cuboidal and a columnar epithelium. We show that Perlecan depletion affects the morphogenesis of the three epithelia, but particularly that of the squamous one, whose planar surface becomes extremely narrow. This defect is due to no other cellular function of Perlecan than its control of the squamous shape of the cells. Furthermore, we find that the lack of Perlecan modifies the structure of the Collagen type IV lattice in the BM of the squamous epithelium, and that the global reduction of Collagen type IV in the Perlecan mutant context substantially restores the morphogenesis of this epithelium. In addition, a stronger decrease in Collagen type IV exclusively in the BM of the squamous epithelium significantly rescues the organization of the two other epithelia. Our data thus sustain a model in which Perlecan counters the rigidity conveyed by Collagen type IV to the BM of the squamous epithelium through the regulation of the assembly of its scaffold, allowing the spreading of the squamous cells, spreading which is compulsory for the architecture of the whole organ.

Key words: basement membrane, Perlecan, morphogenesis, squamous epithelium, tissue mechanics, *Drosophila*

INTRODUCTION

Tissues of epithelial origin constitute the vast majority of animal organs. The variety of their functions are intimately linked to their shape, and changes in the latter can have profound consequences on their physiology and foster many diseases [1]. The architecture of these tissues is maintained throughout adulthood but is established during development, usually via an interplay of forces imposed by the cells themselves and by their extracellular environment, the basal lamina, aka the basement membrane (BM). The generation of internal stress within epithelial sheets largely depends on the mechanical properties of the cytoskeleton and has been under intense scrutiny (see for instance [2]). However, how the external stress applied by the BM governs epithelial organ shape is still an emerging field [3].

The mechanical features of the BM are conferred by its unique composition. Differing from other extracellular matrices, the BM is assumed to be built from two separate meshes arising by the auto-polymerization of Laminin (Lam) and Collagen type IV (Col IV), bridged by Nidogen/Entactin (Ndg) and proteoglycans [4]. Nonetheless, this assembly model has been mostly forged on *in vitro* biochemical experiments using purified subdomains of the aforementioned macromolecules and does not take steric hindrance into account. Moreover, the *in vivo* aggregation of this supramolecular network may induce conformational changes in its structural components, and either create new binding sites among them, or mask some of the identified ones. In support of these concerns, the meshes of Lam and Col IV of the BM of the human skin are tethered by Perlecan, the main proteoglycan of the BM, but not by Ndg [5]. Furthermore, knockouts in mice ascertain a strict requirement for Lam but not the other core constituents in initial BM formation (reviewed in [3], and [6]). Instead, Col IV and Ndg are necessary for the maintenance rather than the incorporation of the other proteins into the BM, and together with Perlecan, for the mechanical stability of the BM as exemplified by its detachment or rupture in the mutant backgrounds. Strikingly, these roles are organ-specific. The majority of these findings are shared with *Drosophila* and *C. elegans* [7-10], with one notable exception: *Drosophila* Col IV is mandatory for Perlecan recruitment to the BM of all tissues examined [11-15]. This may represent a new Col IV function, potentially related to the fact that in this model organism, as well as in *C. elegans*, BM molecules are often produced at a site distant from the BM in which they are incorporated, which could entail a mechanism of BM assembly divergent from vertebrates. Alternatively, this function may have

been concealed in higher organisms, because of increased genetic redundancy. Altogether, these results imply that the biogenesis of the BM varies between tissues. This notion is reinforced by the diversity of its composition, which is connected to the existence of multiple versions of the core components that are differentially expressed depending on the organ and the developmental stage. It is therefore important to continue to expand the repertoire of BMs that are analyzed in order to gain a comprehensive view of their assembly and maintenance, and of the role of this type of matrix in epithelial organ morphogenesis.

Much progress in deciphering the mechanical attributes of the BM and their impact on epithelial tissue shaping *in vivo* has been made in *Drosophila*, thanks to the strong conservation of the main BM elements and the fewer number of genes coding for each protein in flies [16, 17]. In the course of adult ovarian follicle development, this organ changes shape from round to oval. This elongation relies, at least to some extent, on physical forces intrinsic to its BM [18]. Atomic force microscopy (AFM) measurements have revealed that this process is driven by a peak in stiffness in the middle of the BM along the elongation axis, which is contingent on a spatial and temporal gradient of Col IV [18, 19]. In addition, anisotropic BM fibrils containing Lam, Col IV and Perlecan, and that are more rigid than the rest of the BM, are formed across the elongation axis and while they are not sufficient, they may further constrain the tissue [20, 21]. Interestingly, Perlecan displays a distribution that is complementary to that of Col IV, and its uniform overexpression results in the softening of the BM and a decrease in follicle elongation [18, 19]. On the reverse, a reduction in Perlecan levels leads to hyper-elongation [19], but is it unknown in that case if the BM becomes stiffer, as AFM experiments have been hampered by the loss of BM integrity in this context [21]. Overall, these studies demonstrate that Col IV provides tensile strength to the BM whereas Perlecan counteracts this effect, and that a tight balance between these molecules is vital for organ morphogenesis. Similar conclusions have been reached using two other model systems, although AFM has not been carried out. The first one is the neuroepithelium of the brain of the *Drosophila* larva. In this tissue, Col IV and Perlecan also have opposing functions, with Perlecan alleviating the constrictive action of Col IV to maintain proper shape of the brain [11, 22]. In the second model, the larval wing imaginal disc which is the precursor of the adult wing, the same relationship is observed, wherein Col IV is thought to grant tension to the BM, and Perlecan, elasticity. Moreover, this interaction appears to control the degree of stretching along the apico/basal axis of the cells of the columnar epithelium (CoE), which constitutes part of this organ

[11]. Last, confined BM degradation and a local drop in Col IV amount are responsible for the formation of two of the folds of this CoE [23, 24].

Surprisingly enough, the outcome of the genetic manipulation of the BM components on the other cell types of the wing imaginal disc has been neglected. Indeed, this tissue is an epithelial sac with a lumen in its center, consisting of a CoE on one side but of a squamous epithelium (SE) on the other side, and with an intervening cuboidal epithelium (CuE) (Fig S1A). Both the CoE and CuE exhibit a stereotyped folding and the BM is present on the basal side of all three epithelia. Fate maps indicate that CoE cells contribute to the dorsal half of the adult thorax (or notum), the hinge (which attaches the wing to the thorax) and the wing itself, and that CuE cells form the lateral and ventral parts of the thorax (or pleura), while SE cells may give rise to small regions of the pleura, if any [25-27]. Nevertheless, it is known for the SE that it is implicated in growth and identity, and perhaps patterning, of the CoE [28-31], and that it bears a function during metamorphosis. During this process, imaginal discs, that are structures internal to the larva and joined to the epidermis by stalk cells belonging to the SE, become external in a morphogenetic event called eversion [32]. This involves remodeling of the BM of the SE [33], invasion of the epidermis by the stalk cells [27], and expansion followed by retraction/contraction of the other cells of the SE [34]. However, whether the SE and the CuE have fundamental roles in the architecture of the wing imaginal disc, and whether such a role could be exerted through the BM, await to be determined.

In this paper, we use the *Drosophila* wing imaginal disc as a paradigm to consider the function of the BM in the morphogenesis of the three types of epithelia, SE, CuE and CoE, and to understand how their morphogenesis is integrated to sculpt organs as a whole. By focusing on Perlecan, we find that the BM regulates the shape of all epithelia of this tissue and not only that of the CoE. Unexpectedly, we unveil for the first time a role for Perlecan in BM assembly or maintenance, which seems in addition to be curtailed to the SE. We further show that Perlecan ensures appropriate SE morphogenesis not through control of apoptosis or proliferation, but by influencing the shape of its cells. Moreover, we present evidence that Perlecan acts mechanically, by buffering the constraint brought on to the SE by Col IV. Finally, our results strongly suggest that the spreading of the SE prior to eversion is a decisive factor for the architecture of the CuE and CoE, and global tissue morphogenesis. We thus propose that BM-mediated SE morphogenesis is a previously unrecognized mechanism that promotes organ shaping.

RESULTS

Characterization of a new *trol* mutation which impairs wing morphogenesis

We have recently established that the Perlecan of the BM of the wing imaginal disc (thereafter referred as to "the wing disc") is produced autonomously (by the wing pouch CoE) and non-autonomously (*i.e.*, by another tissue), and that there is a partial redundancy between these sources for Perlecan deposition in the BM of this tissue [17]. Therefore, to address the role of Perlecan in epithelial wing disc morphogenesis, but avoid rescue between the autonomous and non-autonomous sources, we attempted to raise animals entirely mutant for a null allele of *trol* (*terribly reduced optic lobes*), the gene encoding Perlecan in *Drosophila* [35]. These animals, however, died between the first and second instar larval stage, precluding their study at the late third instar when the wing disc is fully formed. To bypass this lethality, we used animals entirely mutant for a hypomorphic allele of *trol*. Our attention was drawn to the $trol^{JO271\#49}$ fly line that showed about 80% lethality on the last day of the pupal stage, together with a mispositioned wing phenotype in 38.8% of the mutant pupae (N=125, Fig 1A,B and data not shown). In addition, while some of the viable mutant adults (N=121) were wild-type looking, up to 22.3% of them exhibited wing eversion anomalies (Fig 1C) and 13.2% misshapen wings (not shown), providing a link between Trol and wing morphogenesis.

To further characterize this $trol^{JO271\#49}$ mutant, we analyzed its *trol* locus by PCR and found that a deletion of approximately 5 kb had been created by the remobilization of the G0271 P-element DNA transposon (Fig S1B, see experimental procedures for details). Although the 5' part of this P-element was still present, its 3' end was missing, together with downstream sequences of the *trol* locus comprising the end of intron 9 to the beginning of intron 11. A large number of *trol* mRNA isoforms are predicted in FlyBase (http://flybase.org/), including transcriptional ones. To test the effect of the $trol^{JO271\#49}$ mutant allele on general *trol* expression, we performed RT-qPCR to amplify a sequence predicted to pertain to all isoforms (straddling exons 35 and 36). We found a 91.5% drop in *trol* RNA level in mutant animals (Fig S1C), indicating that the mutation greatly affects overall *trol* expression. To confirm that the $trol^{JO271\#49}$ mutation was ubiquitously reducing *trol* RNA level, we carried out RNA *in situ* hybridization with an antisense probe against *trol* exon 36 [35]. As expected, RNA levels in wing discs from late third instar $trol^{JO271\#49}$ animals were strongly diminished, with no signal detected in the wing pouch (encircled in Fig S1D), and only a

faint signal observed in cells with the highest expression level in wild-type, the adepithelial cells (asterisks in Fig S1D). Likewise in the fat body, an equivalent of the liver and the adipose tissue of vertebrates, and one of the organs that could be synthesizing the non-autonomously produced Trol of the wing disc BM [17, 36], a much weaker signal was seen in mutant animals compared to wild-type (Fig S1E). To appreciate the impact of this decrease in RNA levels on Trol protein synthesis, we stained *trol*$^{JO271\#49}$ animals with an antibody recognizing Trol domain V [37] (Fig S1F). In agreement with the results of the RNA *in situ* hybridization, some Trol was still noticeable in the BM of the fat body of mutant animals, albeit at a lower amount than in wild-type ones. In wing discs, some patchy Trol staining remained in the CuE's BM in the dorsal half of the wing disc, in proximity to the adepithelial cells. Because these cells still produce some Trol, it is possible that this pool diffuses from the adepithelial cells to reach the adjacent CuE's BM. Nevertheless, the staining was inconspicuous in the SE's BM, most of the CuE's BM, and the BM of the wing pouch CoE. Altogether, these data show that this new *trol* mutant allele severely reduces the amount of *trol* RNA and protein, and its late and incomplete lethality makes it suitable for the investigation of Trol function in adult wing and wing disc morphogenesis.

Trol is required for the morphogenesis of the three epithelia of the wing disc

To unravel the function of Trol in epithelial morphogenesis, and since some studies report a role for *Trol* in maintaining epithelial apico/basal polarity [38, 39], we first analyzed the distribution of polarity markers in wing discs from late third instar *trol*$^{JO271\#49}$ animals. The cells, nonetheless, retained normal apico/basal polarity (Fig S2), and in the wing pouch CoE, they displayed an elongated apico/basal (radial) axis (Fig 1D). This phenotype, as well as the globally compact shape of the wing disc along the anterior/posterior axis (Fig 1D,E) is consistent with earlier results achieved with ubiquitous overexpression of an *RNAi* directed against exon 36 of *trol*, or with genetic mutants [11]. Interestingly, we found defects in the *trol*$^{JO271\#49}$ mutant that were not previously described. Indeed, we observed in the pouch CoE ectopic folding on the apical side (Fig 1D and 3C, arrowheads) as well as BM detachment on the basal side (Fig 3D,E, arrows), but these were not penetrant. However, the CuE reproducibly exhibited ectopic folding in the posterior-lateral pleura (Fig 1D, asterisks) and anomalous distribution or packing of the folds of the anterior-lateral and ventral pleura (Fig 1D and 3C-E, respectively). Moreover, the area spanned by the SE

along the anterior/posterior axis was considerably shrunken (Fig 1E). The loss of Trol thus affects morphogenesis of the three different epithelia of the wing disc.

We have shown that the autonomous and non-autonomous sources for the Trol of the wing disc BM cooperate also to sustain proper morphogenesis of this tissue, yet in this study we only focused on the overall shape of the wing disc [17]. To assess the participation of the two Trol sources to the morphogenesis of the three distinct epithelia of this tissue, we examined their morphology in detail after targeting each source using RNAi (*shRNA* against *trol* exon 36) and the *GAL4/UAS* system for tissue-specific expression. Upon *trol* downregulation in the wing disc (with *C765GAL4*), the CuE and CoE appeared normally organized, but the area covered by the SE was slightly decreased (Fig S3B,B',E). The downregulation of the non-autonomous and part of the autonomous *trol* sources (with *PplGAL4*, see [17]) did not elicit very obvious changes in the CoE or the CuE either (Fig S3C). Nevertheless, it led to a more pronounced diminution of the width of the SE, albeit not as severe as in the $trol^{JO271\#49}$ background (Fig S3C',E, compare to Fig 1E). As a deficit in one source might be compensated for by the other one, we simultaneously depleted both sources (with *C765GAL4* together with *PplGAL4*). We now found that the SE was strongly impacted and morphogenesis of both the CoE and the CuE was altered in a way similar to that of the $trol^{JO271\#49}$ mutant (Fig S3D,D',E compare to Fig 1E and Fig 3C-E). These data hence uncover a functional redundancy between the two Trol sources for the architecture of the three types of epithelia of the wing disc, and strengthen the key role of Trol in this process as witnessed with the $trol^{JO271\#49}$ mutant.

Trol regulates the shape of the squamous epithelial cells

The SE is important for disc eversion [27, 32-34]. Because some $trol^{JO271\#49}$ adult escapers display aberrant wing eversion and all mutant wing discs have a prominent SE phenotype, we chose to explore the function of Trol in SE morphogenesis in more depth and identify the mechanism by which its loss triggers a reduction in the area spanned by the SE. This could be due to a smaller cell number, owing to an increase in cell death or a reduction in cell proliferation, two phenotypes associated to the lack of Perlecan (see for instance [39-41]. We first determined the occurrence of apoptosis in this tissue with an antibody recognizing the activated from of Caspase 3, but apoptotic cells were detected neither in the SE of the wild-type late third instar discs (in agreement with [42]), nor in that of the $trol^{JO271\#49}$ (Fig S4A). Second, we tested whether a lower mitotic rate could

underlie this phenotype by performing a staining with and antibody targeting the phosphorylated form of histone H3. At the late third instar stage, SE cells of both control and mutant conditions were unmarked (Fig S4B), in line with the literature describing a very slow division rate for these cells [43]. Last, we analyzed the cell number of the SE in wild-type and *trol*$^{JO271\#49}$ wing discs. Remarkably, this number was not altered in the mutant SE (Fig 2A', quantified in B), ruling out any variations in cell death or proliferation in the absence of Trol.

We therefore envisaged that the shrinkage of the SE of the *trol*$^{JO271\#49}$ wing discs could be explained by a decreased size of its cells. We estimated the volume of this tissue and found that it was smaller than in the control, leading to a higher cell density (Fig 2A, quantified in B). This means that the average cell volume -the value inverse of that of the density- is reduced in the mutant. To establish whether this decrease in size was homogenous along the three axes of the cells, we measured their mean planar surface area. There was indeed a drop in the surface area of the mutant SE cells (Fig S6A,A'), but this drop was more drastic than that of the volume of the cells (approximately 5.3 fold versus 2 fold, respectively). We infer from these results that the diminution of the planar surface area of the cells is partially compensated by an elongation along their radial axis. This was supported by the fact that we noticed that cells of the *trol*$^{JO271\#49}$ SE often had a tendency to be more cuboidal than squamous (Fig 2C). We thought that such a transition in cell shape would be more readily observable in a stronger loss-of-function condition for *trol,* and we thus turned to the ubiquitous overexpression of *trol* RNAi. The wing disc was even more compact along the anterior/posterior axis (Fig 2D') than in the *trol*$^{JO271\#49}$ background. In addition, the SE no longer exhibited its distinctive monolayer of flat nuclei stretching orthogonally to its radial axis, and instead, was replaced by what could be a multi-layered epithelium containing rounded nuclei and cuboidal cells (Fig 2D,D'). To gain more insight into the morphology of the cells, Transmission Electron Microscopy (TEM) was carried out. This revealed that the SE was folded back on itself and that it protruded toward the lumen, forming in some regions a bi-layered epithelium whose cells were clearly cuboidal (Fig 2E, cells from either side of the red dotted lines). This last set of results hence demonstrates that the loss of Trol hinders the flattening of the SE cells.

Trol is crucial for the biogenesis of the squamous epithelial basement membrane

We then sought to investigate whether the impaired morphogenesis of the SE of the *trol*$^{JO271\#49}$ wing discs could arise from a role of Trol in BM formation. We started by evaluating the

consequences of the *trol* mutation on the morphology of the SE's BM. Since the ultrastructure of the BM of the wild-type wing disc has not been described in great detail [44], and Pastor-Pareja and colleagues (2011) limited their study to the BM of the CuE, we undertook the characterization the SE's BM by TEM. The BM of the control SE was thin and homogenous, except for its outer surface that was darker and composed of dots giving it a hairy appearance (Fig S5 and 3A). In the $trol^{JO271\#49}$ wing discs, the SE's BM was clearly abnormal: its thickness was decreased by half (Fig 3A, brackets, quantified in B), and there was a number of regions where it was reduced to a thread (the "hairy" outer layer), no longer in contact with the cell surface (Fig 3A, arrow). Nonetheless, this BM was never absent nor ruptured. These data therefore indicate that whereas Trol is not required for the SE's BM integrity in this hypomorphic background, it is involved in another aspect of its biogenesis.

To address whether the changes seen by TEM could stem from a function of Trol in the assembly or maintenance of the SE's BM, we looked at the incorporation of the other main BM structural components, Lam, Ndg and Col IV. Others have found that Trol is not needed for Col IV deposition in the wing disc, yet their analysis was restricted to this component and to the CuE of the posterior ventral pleura [11]. Upon examination of the three BM components, we did not detect any modification in their expression pattern in the BM of the CoE or most of the CuE of the $trol^{JO271\#49}$ wing discs (Fig 3C-E and not shown). However, at the level of the SE' BM and the posterior portion of the lateral CuE closest to the SE, although incorporation of Lam in the mutant remained similar to wild-type (Fig 3F), both Ndg and Col IV distribution were affected (Fig 3G). Fibril-like structures parallel to the anterior/posterior axis appeared in negative in the Ndg layer by antibody staining and by direct visualization of a GFP-tagged Ndg (not shown), likely reflecting a depletion rather than a conformational change. Conversely, positive fibril-like structures were seen for Col IV, also running in the same orientation. Furthermore, the positive and negative fibril-like structures overlapped (Fig 3G, arrows). It has been published that the absence of Ndg in the wing disc BM does not impinge on the integration of the other BM components [15], which we confirmed for Col IV at the level of the SE BM (not shown). This thus shows that Trol is the primary factor responsible for proper assembly and/or maintenance of the Col IV network. Whether Trol is necessary for proper incorporation and/or maintenance of Ndg in a direct way or through Col IV still needs to be elucidated. Anyhow, these results expose for the very first time a role for Trol in epithelial BM biogenesis, but a role that is mainly confined to the BM of the wing disc SE.

Trol controls the mechanical properties of the squamous epithelium through Col IV

As Trol has been proposed to promote BM elasticity [11, 18], and a decrease in this elasticity might be relayed to the underlying cells and affect their spreading, we first studied the orientation of the cells of the SE (Fig S6C). In wild-type wing discs, the direction of the major planar elongation axis of the cells had a tendency to become tangentially oriented toward the periphery, such that posterior-most cells were aligned parallel to the dorsal/ventral axis and ventral-most cells were aligned parallel to the anterior/posterior axis. Nevertheless, it was isotropic in the center of the tissue. In contrast in the *trol*$^{JO271\#49}$ SE, with the exception of ventral-most cells, the orientation of the major elongation axis of the cells was anisotropic and parallel to the dorsal/ventral axis. It hence appears that in the absence of Trol, there is a lessening of the spreading of the tissue parallel to the anterior/posterior axis.

Col IV provides tensile strength to the BM [18, 45] and its assembly into anisotropic fibrils in the ovarian follicle imparts extra stiffness to the BM, participating to the constraint of the tissue expansion parallel to the direction of these fibrils [21]. Because aberrant Col IV fibril-like structures running along the anterior/posterior axis are seen in the *trol*$^{JO271\#49}$SE, it is possible that they generate a raise in BM tension, constricting the tissue in this axis. To examine this, we appraised the pattern of mechanical stress of the SE by following the tissue deformation consecutive to an *ex vivo* laser-slit perpendicular to the anterior/posterior axis. The SE was identified by the spacing of its nuclei (marked with His2AV-GFP) and a slit was made in its central cells orthogonally to the anterior/posterior axis, *i.e.*, parallel to the dorsal/ventral axis ("D/V slit", Fig 4A). Since SE's nuclei are set far apart in the wild-type, there were not enough of them in the vicinity of the slit to get a reasonable sampling of their displacement. As an alternative, we tracked more abundant intracellular granules detected by transmitted light. We found in the control condition that this D/V slit produced a negligible deformation (Fig 4B, quantified in C). Strikingly in the *trol*$^{JO271\#49}$ mutant, an anisotropic deformation of the SE after the slit was now obtained, as granules moved away from the slit, and essentially orthogonally (Fig 4B'-C'). We deduce from these data that the loss of Trol causes an abnormal constriction of the tissue along the anterior/posterior axis, in accordance with the failure of its cells to spread parallel to this axis (Fig S6C). Taken together, our results strongly argue in favor of a direct mechanical function for Trol, which is to confer to the SE the ability to expand.

As stated above, it is conceivable that the anomalous distribution of Col IV in the BM of the SE of *trol*$^{JO271\#49}$ wing discs accounts for the defective morphogenesis of this tissue. To tackle this hypothesis, we lowered the amount of Col IV in the *trol*$^{JO271\#49}$ mutant by introducing in this context one copy of a hypomorphic allele of *Viking* which encodes one of the two alpha chains of Col IV [46]. This reinstated the isotropy of the major planar elongation axis of the cells of the SE (Fig S6D) and did elicit changes in its surface area, as it was evidently widened (Fig 5A,B, quantified in C). Interestingly, despite the fact that the basal surface of the CoE was not expanded (Fig 5A',B',C), the folding of all parts of the CuE was more similar to wild-type, yielding on the whole discs that were much more relaxed (Fig 5A''-B'''). Moreover, pupal wings were no longer mispositioned and both lethality and adult wings phenotypes were substantially rescued (Fig 5D). These data therefore indicate that the role of Trol in SE morphogenesis and in adult wing formation and viability, are Col IV-dependent.

Trol controls epithelial tissue architecture via control of squamous epithelial morphogenesis

Finally, as the effect of Trol loss on the incorporation and/or maintenance of Col IV and Ndg is mostly restricted to the SE's BM, we reasoned that the abnormal architecture of the two other epithelia observed in the *trol*$^{JO271\#49}$ wing discs might be the sole consequence of the deficient SE morphogenesis. We could not test this possibility by specifically removing Trol from the SE's BM, because this Trol originates from two sources that also provide Trol to the BM of the CuE and CoE [17]. To circumvent this problem, we opted for the opposite approach, which was to attempt to specifically rescue the SE's phenotype of the *trol*$^{JO271\#49}$ mutant discs and assess the outcome on the rest of the tissue. Since the constraint on the mutant SE is exerted through Col IV, we decided to lower the amount of Col IV in the SE's BM by directing the expression of the Col IV-cleaving matrix metalloprotease MMP2 to this epithelium with the *GAL4/UAS* system. We used *CoroGAL4*, one of the few *GAL4* lines reported to allow expression in the SE but not in the CuE or the CoE of the wing disc [30, 47].

We started by expressing MMP2 with *CoroG4* in wild-type discs. This did not compromise the organization of any of the epithelia of the wing disc, aside from triggering a small tear in the SE at the border with the anterior CuE (not shown). This finding entails the existence of a local difference in rigidity in this region, and that the BM of the SE bestows it with resistance to withstand mechanical strain. We subsequently induced the expression of MMP2 in *trol*$^{JO271\#49}$ wing

discs and stained them for Ndg. As expected, the CuE and CoE BMs were intact in these samples but the SE's BM was disrupted by MMP2 (Fig 6, compare C' to B' and C to B, respectively). Furthermore, the SE itself was totally ruptured, an aggravation of the phenotype seen in wild-type discs, which points to a reduction in elasticity of the SE in the *trol* mutant. Nonetheless, the area covered by what was left of the SE was greatly expanded and similar to wild-type (Fig 6, A-C and A''-C'', quantified in D). Remarkably, the wing disc was less compacted along the anterior/posterior axis (Fig 6, A'-C' and A''-C'', quantified in D) and the folds of the different regions of the CuE, even if not fully restored to their normal distribution, were more relaxed (Fig 6, A''-C'' and A'''-C'''). On the other hand, the confined expression of MMP2 to the CuE and CoE (with *C765GAL4*) did not save the $trol^{JO271\#49}$ phenotype and gave rise to grossly de-structured wing discs (not shown). These results thus show that the Trol-dependent morphogenesis of the SE dictates wing disc architecture.

DISCUSSION

Role of Trol in squamous epithelial BM assembly

So far, the literature ascribes a role for vertebrate and invertebrate Perlecan in granting developing and adult epithelial organs with resistance to mechanical stress. This is at best correlated with a function for Perlecan in insuring BM integrity, and there is as yet no *in vivo* clue that Perlecan is vital for initial epithelial BM formation [11, 18, 19, 21, 22, 48-51]. Even in considering tissues of mesodermal origin, there is only one account for Perlecan being needed for the correct localization of Ndg in the BM of *C. elegans* muscles [52], and another one where it organizes lam and Col IV in a very specialized scaffold of BMs internal to the *Drosophila* lymph gland [53]. Here, we have reexamined the role of Perlecan in epithelial BM biogenesis.

Using the *Drosophila* wing disc, we discovered in the $trol^{JO271\#49}$ animals that a decrease in Trol leads to a partial detachment of the BM from the SE of this organ. Still, this BM is not broken nor it disappears (Fig 3A), a phenotype only witnessed upon Trol depletion through ubiquitous expression of an RNAi (not shown). This suggests that the preservation of the integrity of the BM in our model system is the outcome of a more upstream requirement for Trol in BM assembly. Indeed, while Lam, Ndg and Col IV are homogenously deposited in the BM of the wild-type SE, Col IV consistently forms anisotropic fibrils which are matched by Ndg negative ones following loss of Trol (Fig 3G). Consequently, Trol appears necessary for creating a stable network of Ndg and Col IV. Based on biochemical experiments, it might do so by directly interacting with these two proteins, or, as Ndg and Col IV can also bind to each other, its effect on one of these components might be indirect and mediated by the other one [4]. *In vivo* studies in *Drosophila* indicate that Ndg is not critical for Col IV recruitment to BMs, and vice-versa, except in the fat body where these molecules depend on one another for their proper distribution [8, 15]. Since the contribution of Col IV to the biogenesis of the BM of the SE has not been clearly established, it will still have to be elucidated to understand how Trol impacts Ndg incorporation. However, we found that the lack of Ndg did not alter Col IV integration into this BM (not shown), implying that Trol directly acts on Col IV.

One puzzling aspect of our work is that the Lam lattice does not seem to be affected by the reduction of Trol (Fig 3C,F). Although we cannot dismiss modifications undetected by our experimental set-up, this is in agreement with the vast majority of the data reporting that Lam does

not rely on the other core proteins for its deposition into the BM [4]. Nevertheless, this implies that the generation of Col IV fibrils in the mutant context does not hinge on the generation of such structures in the Lam layer. Interestingly in *Drosophila*, it has been shown that Lam is dispensable for BM formation at embryonic muscle attachment sites [7], and that the targeting of Col IV to the BM of the larval epidermis after wounding does not need Lam [54]. Moreover, Col IV is directed at the BM of the *C. elegans* pharynx by apparently bypassing Lam, a process that involves RGD-binding Integrin cell surface receptors [55]. Because Perlecan contains RGD motifs, including in *Drosophila*, and can be linked to Integrins [56], it is therefore plausible that its absence liberates Integrin binding sites and favors this alternate pathway of Col IV recruitment. This warrants further investigation and could offer valuable insights into the regulation of these distinct modes of BM assembly.

Another surprising feature of our results is the presence of anisotropic Col IV-positive fibrils in the BM of the SE in the *trol* mutant. This brings up the question of how the loss of Trol prompts their biogenesis. Col IV is a reticular collagen that consist of a helix with an NC1 globular domain on one end and a 7S domain on the other. It trimerizes to form a so-called “protomer”, which in turn polymerizes via homotypic NC1 and 7S interactions. This mesh is then reinforced by covalent bounds at both the NC1 and 7S interface that are catalyzed by two different enzymes, providing a spread-out scaffold [57]. Nonetheless, another more irregular network can also form via lateral interactions between the triple helix of the protomers [58]. It is hence tempting to propose that Trol promotes the covalent cross-linking of the Col IV lattice and/or restricts the lateral associations, and that in its absence, the latter increase dramatically, triggering a collapse of the network. In addition, NC1 fragments can stem from extracellular Col IV proteolysis [59], which could change the association of Col IV with its partners, as well as impair its polymerization or weaken the stability of its mesh. It will thus be worth seeing if the Col IV fibrils are specifically devoid of this NC1 domain, as this would again shift the balance toward lateral interactions. Moreover, it will be important in the future to genetically manipulate the enzymes responsible for the NCI proteolysis and the covalent bounds, and to engineer a version of Trol deleted of its potential binding domain to the triple helix of Col IV [60].

Concerning the anisotropy of the Col IV fibrils, clonal analysis shows that cells of the SE freely divide along the dorsal/ventral axis but not along the anterior/posterior axis, since there is a frontier between the SE and the anterior CuE that cells do not cross [43, 61]. This compartment

boundary probably imposes an anisotropic constraint, as underlined by the rupture of the wild-type SE in this region upon its BM degradation with MMP2 (not shown). As just discussed, we think that the lack of Trol undermines the Col IV scaffold. Therefore, the lateral displacement of the SE cells toward the posterior CuE and CoE [43] could yield a mechanical strain along the anterior/posterior axis that could explain the alignment of the Col IV fibrils parallel to this axis, and it will be exciting to precisely map the directionality of the proliferation of the SE cells.

Altogether, our data expose for the first time an *in vivo* role for Perlecan in the incorporation or maintenance of the core components Ndg and Col IV in an epithelial BM. In mice, Perlecan is mandatory for the generation of the fibrillary Col II scaffold in the extracellular matrix of the cartilage [48, 62], and for the accumulation of acetylcholinesterase at the synaptic BM by interacting with its collagen-like tail [63]. It hence appears that Trol has an analogous function to that of vertebrate Perlecan, the common denominator being the organization of collagen networks.

Role of Trol in the physical properties of the squamous epithelial BM

We performed TEM on the BM of the SE and discovered a general twofold drop in its thickness in the *trol*$^{JO271\#49}$ animals (Fig 3B). This could be brought about by the loss of Trol as a tethering molecule that would normally enhance the physical distance between the Lam and Col IV meshes. Furthermore, the negatively charged glycosaminoglycan chains of proteoglycans bind water, controlling both BM thickness and elasticity [64]. Such a role has not been uncovered by the targeted deletion of the three main sites for heparan sulfate (HS) chains substitution in the domain I of mouse Perlecan. However, this mutant protein still bears HS and chondroitin chains in another domain, and redundancy with the Col XVIII proteoglycan has been described [49, 50]. In *Drosophila*, Col XVIII is not present in the BM of the SE (our unpublished results), and the other major proteoglycan of the BM Agrin does not exist. Because we have recently demonstrated that the HS attachment sites of Trol are conserved in this species [17], Trol could be the primary factor controlling the hydration of the SE BM, and therefore its thickness and elasticity. Two lines of evidence emphasize that Trol acts mechanically to determine the thickness of the BM in our model system. First, our laser surgery experiment indicate that the SE is more constricted in the *trol*$^{JO271\#49}$ animals, likely reflecting a stiffer BM (Fig 4). Second, the reduction of the amount of Col IV in the *trol* mutant in two separate conditions reinstates proper SE morphogenesis (Fig 5 and 6). Interestingly, Perlecan can be connected to Col IV both *in vitro* and *in vivo* by its HS chains [5,

65]. Since Col IV confers rigidity to the BM, we thus propose that the prime function of Trol is to supply the SE BM with elasticity, via the control of the assembly of the Col IV lattice through its HS chains.

Specificity of the role of Trol in squamous epithelial BM biogenesis

Strikingly, the BM of the CuE and the CoE of the *trol*$^{JO271\#49}$ wing discs did not exhibit obvious defects in the incorporation or maintenance of the other structural components (Fig 3C-E and not shown). This points toward a lack of role for Trol in the biogenesis of these BMs, and fits with the idea that there exists tissue-specific requirements for BM formation in *Drosophila*. This specificity is assumed to be due to a heterogeneity either in the source of the BM molecules (autonomous versus non-autonomous) that could bestow differences in BM assembly, and/or in its composition [15]. With respect to the source-based hypothesis, we found that Trol is both autonomously and non-autonomously produced for at least its integration in the BM of the SE and the CuE of the wing disc [17], implying that the mechanism of Trol deposition is the same in these two regions of the BM. We nevertheless do not reject the possibility that the source for the other core proteins may vary according to the type of epithelium to which the wing disc BM is associated, and this would have to be thoroughly inspected. Concerning the diversity in BM composition, all four main components localize to the entire BM of the wing disc (Fig 1D and 3C-E). This does not rule out local quantitative fluctuations in their distribution, and that the repertoire of accessory molecules, such as the enzymes involved in the maturation of the Col IV scaffold, changes along the BM. Differences in BM composition in the wing disc are actually corroborated by our TEM studies. While the BM beneath the SE and the CuE is similarly dense, the BM of the CuE is thicker than that of the SE, and the BM under the CoE of the pouch is lamellated and even thicker (Fig S5 and our unpublished data). These divergent morphologies highlight the existence in the wing disc of not one, but three BMs, with unique traits and specific to the epithelial type they abut. Unlike the CuE and the CoE, the SE endures extreme stretching during eversion [32, 34], and as such, is the one that demands the most compliant BM. Because Trol provides elasticity to the BM [18], it is therefore conceivable that the biogenesis of the BM of the SE is distinct from that of the CuE and CoE, and more sensitive to the loss of Trol.

Alternatively, Trol could hold a function in the formation of the two other BMs that is concealed by redundancy. As stated above, Col XVIII is absent from the BM of the SE, and we did

not detect it either in the BM of the CuE. Nonetheless, and alike to Trol (Fig S5B'), it is enriched in the BM underneath the folds of the pouch CoE (our unpublished results), and could compensate for Trol in the hydration of this BM and also as an organizer of the Col IV network [66]. In addition, another molecule that could fulfill Trol role is Ndg. Indeed, *Drosophila* Ndg is not essential for BM formation and integrity in most tissues [8]. However, the concomitant elimination of Ndg and Trol leads to pupal lethality, a phenotype that is not seen in either mutant alone [15]. Hence, a redundancy with Ndg could account for the normal BM assembly of the CuE and the CoE of the wing discs of the *trol* mutant. In conclusion, it will be crucial to undertake the analysis of wing discs in which Trol is depleted together with Col XVIII or Ndg, to distinguish between a limited versus a broader function for Trol in epithelial BM biogenesis.

Role of Trol in squamous epithelial morphogenesis

Perlecan knockout in mice causes exencephaly [67], but none of the attributes of the brain neuroepithelial cells are manifestly disturbed [48]. In mice deficient for both Col XVIII and the HS chains of Perlecan, the epithelial cells of the lens develop an invasive behavior and display ectopic cell death, revealing that Perlecan inhibits cell migration and behaves as a survival factor in this organ [49]. This second role is conserved in the human skin where PERLECAN protects the regenerative keratinocytes from apoptosis [40]. Presumably owing to lesser genetic redundancy, work in *Drosophila* hints toward a need for Trol at an earlier step of epithelial morphogenesis, but with conflicting findings. In the adult gut and the follicular epithelium, loss-of-function clones for the null allele of *trol* alter the polarity of the cells [38, 39], but the second result could not be confirmed [68, 69]. Moreover, in a model of tumorigenesis in the wing disc, Trol induces epithelial neoplasia in lieu of sustaining polarity [70]. Thus, our comprehension of the role of Perlecan in epithelial morphogenesis is fairly poor, particularly in that of the squamous sort, since the aforesaid studies do not focus on SE.

Here, the use of a hypomorphic allele of *trol* has allowed us to disclose a function for Trol in SE morphogenesis which could have been otherwise masked by a more complex phenotype elicited by a stronger allele. With the $trol^{JO271\#49}$ allele, cell polarity was not compromised as a whole (Fig S2), and neither was cell survival nor proliferation in the SE (Fig S4 and 2B). Instead, we determined that the more prominent defect in this epithelium is a change in cell shape. The comparison between the wild-type and mutant SE cells of the average cell volume (Fig 2B) and

surface area along the planar axis (Fig S6A,A'), shows that the mutant cells have a reduced planar surface and suggest they have an increased radial axis. This means that their squamous morphology is affected in this background, and some cells, although not all, are clearly cuboidal in shape (Fig 2C). Nevertheless, a full conversion of the SE to a CuE is achieved by the ubiquitous overexpression of *trol* RNAi (Fig 2D-E). These data therefore unveil a novel role for Trol and the BM in the control of the squamous morphology of cells.

The activation and repression of a few pathways has been described to instruct epithelial cells of the wing disc toward a squamous fate [31, 47]. The cuboidal shape of the cells witnessed upon the loss of Trol could hence reflect a change in their identity. This does not seem to be accurate, first because the promotors of the *AGiR* and *Coro* genes that are normally expressed in the SE are still active in the $trol^{JO271\#49}$ wing discs (Fig 1E, 2A and 6C), and second, because the number of cells in the domain of *AGiR* transcription is the same as in the control (Fig 2B). Besides, modification of epithelial cell morphology without modification of fate is not unprecedented as for example, the outer layers of the transitional epithelium of the urinary tract flatten and turn squamous once the urinary compartments are filled.

Another possibility is that the abnormal shape of the mutant cells is somehow related to their smaller size (2 fold drop in their volume, from our analysis of Fig 2B). We nonetheless do not believe it to be the case for the following reasons. On one hand, this size variation may not be connected to a growth defect and could be a consequence of the change in cell shape rather than its origin, since cells do not necessarily conserve their volume during this process [71, 72]. Furthermore, the lack of Trol does not impinge on cell growth in the CoE of the wing imaginal disc [73]. On the other hand, the shrinkage of the amnioserosa, a SE in the *Drosophila* embryo, is driven by a decrease in its cells volume [74], but unlike in our experiments, it is provoked by apoptosis and does not entail an elongation of their radial axis.

Last, the function of Trol could be to grant a mechanical environment propitious to the spreading of the SE cells. This is substantiated by many of our observations. Indeed, the basal surface of the SE of the wild-type and $trol^{JO271\#49}$ wing discs is different upon 3D reconstruction (Fig 2A), the former being wiggly, and the latter being straight. This implies that in the mutant SE, the mechanical tension of the cells is altered. In addition, SE cells partially detach from their BM (Fig 3A), which could be caused by a raise in their basal tension. Moreover, the major planar elongation axis of the mutant cells becomes anisotropic and parallel to the dorsal/ventral axis (Fig

S6C), denoting an impeded ability of these cells to spread along the anterior/posterior axis. This points to an increase in their constriction in this second axis, which is validated by our laser surgery experiment (Fig 4C'). Furthermore, we found that Col IV fibrils aligned parallel to the anterior/posterior axis are generated in the SE of the *trol*$^{JO271\#49}$ wing discs (Fig 3G), and that the reduction of the planar surface area of these cells, the orientation of their major elongation axis, as well as all their spreading along the anterior/posterior axis, all depend on this component (Fig S6B,C, Fig 5A,B,C and Fig6A,B,C,D). Remarkably, a softening of the BM is required for one of the cell populations of the ovarian follicle to undergo a transition from a cuboidal to a squamous shape [21]. Thus, we propose that the absence of Trol generally stiffens the BM of the SE, interfering with the spreading and flattening of its cells, which are initially cuboidal [43], and that again akin to the follicular epithelium, the formation of polarized Col IV fibrils further enhances the rigidity of the BM along the anterior/posterior axis, constraining cell expansion in this direction even more.

Role of Trol in organ architecture

Our study presents evidence that Trol orchestrates overall wing disc morphogenesis, because it controls the morphogenesis of the SE, but also that of the CuE and CoE (Fig 1D,E, 3C-E and S3). In the *trol*$^{JO271\#49}$ wing discs, the cells of the pouch CoE have an elongated radial axis, as previously published [11], but they also exhibit non-penetrant detachment from their BM and ectopic apical folding. In addition, in the CuE, reproducible ectopic apical folding and anomalous packing of the folds are seen. The ectopic apical folds cannot easily be accounted for by currently known mechanisms. In the leg disc CoE, apical folding is fostered by a local concentration of apoptotic cells [75]. However, we did not detect cell death in any of the epithelia of the Trol mutant wing disc (Fig S4A). In the wing disc CoE, a restricted decrease in BM components is associated with the generation of two apical folds bordering the pouch and one apical fold in the hinge [23, 24]. Yet, our analysis of the expression of the core proteins of the BM of the Cue and CoE did not expose obvious alterations in their pattern, and intriguingly, it was the biogenesis of the SE BM that was the most overtly compromised (Fig 3 and data not shown). This led us to hypothesize that the abnormal Col IV network of the SE BM was responsible for the generally defective organ architecture, which we tested by specifically degrading Col IV in the SE of the *trol*$^{JO271\#49}$ wing discs. We found that this treatment restored the area spanned by both the SE and the basal side of

the CuE and CoE of the pouch region along the anterior/posterior axis (Fig 6). This therefore indicates that the expansion of the SE parallel to this axis is paramount to the relaxation of the two other epithelia.

Based on these results, we propose that in the *trol*$^{JO271\#49}$ wing discs, the Col IV-mediated constriction of the SE in the direction of the anterior/posterior axis directly exerts an excessive basal tension on the nearby CuE, which in turn is transmitted to the CoE. This would trigger a reduction of the basal surface of the CuE and CoE cells, as reported for the latter [11]. In the case of the CoE cells, this change could cause their occasional detachment from the BM, since their basal domain is normally already narrower than that of the CuE cells, making them less able to withstand mechanical stress. For both type of epithelia, the repercussion of the drop in the basal area of their cells would be an increase of the length of their radial axis, and/or an increase of the surface of their apical domains, as observed for the CoE cells [11]. A concomitant decrease and enlargement of the cells basal and apical domains, respectively, creates wedge-shaped cells and could definitely be the reason for the ectopic folding of the CoE and the CuE (see for instance lower asterisk in Fig 1D). Last, an expansion of the apical surface of cells could explain the abnormal packing of the folds of the CuE, because a compaction of the tissue would allow to accommodate for this increase within the boundaries of a closed environment. This last aspect of our model is best illustrated by the morphology of the wing disc in which Trol is ubiquitously depleted using RNAi, as all epithelia display numerous ectopic folds which are extremely packed (Fig 3D',E).

We are aware of at least two SE that operate as regulators of organ development, but are fated to disappear before adulthood. The first one is the *Drosophila* amnioserosa, whose contraction and apoptosis is vital for the closure of the adjacent embryonic epidermis [76]. The second one is the mouse periderm which covers the embryonic epidermis and is shed prior to birth, but is needed to avoid epidermal fusion of digits after interdigital cell death [77]. Our work hence provides another example of a SE, that of the *Drosophila* wing disc, which by interacting with another epithelium is instrumental for tissue architecture. We believe that the pursuit of the role of Perlecan and the BM in SE morphogenesis in other contexts will be invaluable to better comprehend the morphogenesis of complex epithelial organs.

EXPERIMENTAL PROCEDURES

Drosophila strains and genetics

Mutant alleles were *Vkg*^{01209}, *trol*$^{JO271\#49}$ characterized here, and *trol*^{GO271}. *UAS* lines were: *UAS-trol.RNAi*^{JF03376} (TRiP collection), *UAS-Mmp2*, *UAS-GFP* and *UAS-Dcr-2*. *GAL4* lines were: *Act-GAL4*, *ppl-GAL4*, *AGiR-GAL4*, *C-765-GAL4* and *coro-GAL4* [30]. To modulate GAL-mediated expression of UAS transgenes, we used *tub-GAL80*^{ts}. Additional lines were *His2Av-EGFP*, the GFP protein trap line *vkg-GFP* [78] and *Ndg-sGFP* from the VDRC. *w*^{1118} served as a wild-type control. Non-referenced lines were obtained from the BDRC.

Flies were raised on standard cornmeal-agar medium and crosses were performed at 25^{0}C except for time-controlled experiments. Time-controlled expression of *Mmp2* was achieved by crossing flies carrying the *trol*$^{JO271\#49}$ allele and *Mmp2*, with flies carrying *coro-GAL4* together with *tub-GAL80*^{ts}. Crosses were maintained at 18°C (GAL80^{ts} permissive temperature) until the middle of the late third instar larval stage (9 days), and then switched at 29°C (GAL80^{ts} restrictive temperature) for 24h prior to dissection. For time-controlled expression of *GFP*, flies carrying *AGiR-GAL4* or *coro-GAL4* or *Ubx-GAL4,* together with *tub-GAL80*^{ts}, were crossed to flies carrying the *UAS-GFP* construct. Crosses were maintained at 18°C until the mid third instar larval stage (8 days) and then switched at 29°C for 24h prior to dissection.

Molecular characterization of the *trol*$^{JO271\#49}$ allele

The *trol*$^{JO271\#49}$ mutant line was issued from the genetic screen that generated the *trol*^{null} allele [35]. This screen was designed to obtain a large genomic deletion following concomitant mobilization of two P-elements flanking exon 10 and the last *trol* exon, exon 56. Since *trol* is on the X chromosome, the *trol*$^{JO271\#49}$ allele was characterized by isolating genomic DNA from adult hemizygous mutant male escapers (as described in [79] and mapping of the region surrounding the two P-elements by PCR. The 5' located P-element (G0271), but not the 3' one, was improperly excised creating a deletion. The breakpoints of this *trol*$^{JO271\#49}$ deletion were verified in two independent PCR reactions, and genomic DNA extracted from *w*^{1118} and heterozygous *trol*^{GO271} adult female flies served as positive controls for PCR amplification. Primer sequences are available upon request.

Characterization of pupal and adult *trol*$^{JO271\#49}$ phenotypes

To observe pupal wing phenotypes and determine the stage at which lethality occurs in the *trol*$^{JO271\#49}$ mutants, 25 virgin females were crossed with 10 males of a fly stock carrying the *trol*$^{JO271\#49}$ allele balanced over a GFP-expressing FM7 chromosome, and left to lay eggs on agar plates for 4h. 24h later, mutant male larvae were picked on the basis of their lack of GFP expression and transferred to a vial, with a maximum of 50 larvae per vial. These were then daily retransferred to a new vial and counted until puparium formation. After pupariation, pupae were examined for lethality and wing phenotypes on a daily basis until eclosion. *w*^{1118} served as controls.

To assess the rescue of the lethality and wing phenotypes of *trol*$^{JO271\#49}$ mutant adult males by the introduction of one copy of the mutant allele *Vkg*^{01209} in the background, 10 virgin females carrying the *trol*$^{JO271\#49}$ allele balanced over the GFP-expressing FM7 chromosome were crossed to 6 males, either carrying the GFP-expressing FM7 chromosome, or carrying the GFP-expressing FM7 chromosome together with the *Vkg*^{01209} allele balanced over a GFP-expressing Cyo chromosome. These crosses were set in parallel and kept in vials, and parents were transferred every 24h to new vials for at least 6 days in a row. For each vial, flies of the relevant genotypes as well as their wing phenotypes were scored on a daily basis during 10 days following the beginning of eclosion.

For pictures, pupae were first collected with a paint brush and gently washed in water. Bright field images of pupae and adult flies (*w*^{1118} or *trol*$^{JO271\#49}$ males) were taken on a wide-field Axioplan2 Zeiss microscope equipped with a color camera. Pictures were processed with the Adobe Photoshop CS6 software.

RT-qPCR

Total RNA from 20 late third instar larvae (*w*^{1118} or *trol*$^{JO271\#49}$ males) was extracted with the TRI Reagent (MRC) and cDNA was synthesized by random-priming with the Superscript III First-Strand Synthesis System (Invitrogen), starting from 2µg of RNA. 8 ng of cDNA were used to perform real time RT-PCR with the PowerSYBRGreen PCR mastermix (Applied Biosystem) and StepOne Plus (Applied Biosystem). Samples were normalized with the house keeping gene Actin. At least three separate samples were collected per experiment and triplicate measurements were run on each sample. PCR conditions, primer sequences and sequences are available upon request.

***RNA in situ* hybridization**

Sense and antisense probes for *trol* mRNA were designed against the largest *trol* exon as in [35], and synthesized with a DIG RNA Labeling Kit (Roche). Whole-mount RNA *in situ* hybridization on larval tissues was carried out essentially as described in [80] except that fixed dissected larvae were dehydrated in methanol, omitting ethanol and xylene steps, samples were treated with proteinase K at a concentration of 12.5 µg/ml for 30s, and hybridization temperature was 55°C. Probes were detected using an alkaline phosphatase-conjugated anti-DIG antibody and the NBT/BCIP substrate (both from Roche). Samples were mounted in VECTASHIELD (Vector Laboratories). Bright field images were taken on a wide-field Axioplan2 Zeiss microscope using a color camera. Pictures were processed with the Adobe Photoshop CS6 software.

Fluorescent immunostaining

Late third instar larvae were fixed in 4% PFA in PBS, permeabilized with 0.1% Triton X-100 PBS and blocked in 0.1% BSA, 0.1% Triton X-100 PBS. Primary antibodies were diluted as follows: rabbit polyclonal anti-Trol [37] 1:3500, rabbit polyclonal anti-GFP (Torrey Pines Biolabs, TP401) 1:400, mouse monoclonal anti-GFP (Roche, 11814460001) 1:200, rabbit polyclonal anti-Nidogen [81] 1:1000, rabbit polyclonal anti-Lamininβ1 (Abcam, ab47650) 1:500, mouse monoclonal anti-Multiplexin [82] 1:250, rat polyclonal anti-DE-cadherin (Development Studies Hybridoma Bank University of Iowa – DSHB, DCAD2) 1:50, rabbit polyclonal anti-PKCζ (Santa Cruz, sc-216) 1:500, mouse monoclonal anti-Disc large (DSHB, 4F3) 1:100, rabbit polyclonal anti–cleaved Caspase 3 (Cell Signaling, 9661) 1/200, and rabbit polyclonal anti-phospho-Histone H3 (Merckmillipore, 06-570) 1:400. Fluorescent secondary antibodies were diluted at 1:100 (Cy5-conjugated antibodies were from Jackson ImmunoResearch Laboratories and Alexa Fluor 488-, 532- and 647-conjugated antibodies were from Life Technologies). TRITC-conjugated phalloidin (Sigma) was always included at 1:100 in the staining procedure. Samples were mounted in VECTASHIELD with DAPI (Vector Laboratories). To compare specimens of different genotypes, samples were stained in parallel using the same antibody solutions, or in the same tube when tissue morphology allowed them to be distinguished, and imaged with identical acquisition settings. Confocal data were acquired on a Zeiss LSM 780 NLO inverted microscope, and on three different upright microscopes: a Leica TCS SP1, a Leica DM TCS SPE and a Leica TCS SP5. xyz and xzy images were all single sections collected at the focal plane indicated in the figures, except for the xyz images related to the analysis of the squamous epithelium volume and nuclei number and the

squamous cell surface area and orientation axis (see relevant sections of the experimental procedures). Pictures were processed with the Adobe Photoshop CS6 software. No less than 20 wing discs were examined per genotype.

Transmission electron microscopy

Reports of *Drosophila* adult and larval haemolymph osmolarity show highly variable results. Based on the osmolarity of a medium compatible with wing disc culture (from 285 to 345 mosm, [83], we opted for a fixation buffer with an osmolarity of 300 mosm (1.5% glutaraldehyde in 0.075 M cacodylate buffer). Wing discs were then embedded in Epon according to standard procedures. 70 nm-thick sections deposited on slot grids (to prevent parts of the tissue section to be hidden by the mesh present on regular grids) were observed at 100 kV with a 120 kV JEOL JEM-1400 electron microscope. Digital acquisitions were made with a numeric MORADA camera (Olympus SIS). Sectioning and microscope observation was performed at the CCMA EM core facility (Université Côte d'Azur).

BM thickness was analyzed on 2 non-consecutive sections from 3 different discs per genotype, using the straight line tool from ImageJ-win64. 5 images per section were taken at the appropriate location and BM was measured at 2 distinct positions on each image, yielding a total number of 60 values per condition. Note that regions were the plasma membrane bi-layer and the darker outer hairy layer of the BM were not clearly defined were not taken into account as they result from a tangential sectioning of the tissue.

Analysis of the squamous cells area and elongation axis

Following Anti-Dlg staining, Maximum-Intensity projections of z-stacks encompassing the entire SE of the wing disc (step size of 0.42 µm) were processed to produce hand-corrected TIF skeleton images depicting cell outlines with Tissue Analyzer [84]. Skeleton images were analyzed to obtain cell surface area measurement and the cell major elongation axis with Epitools Icy plugins [85].

Analysis of the squamous epithelium volume and nuclei number

Late third instar *wt* or *trol*$^{JO271\#49}$ male larvae expressing a *UAS-GFP* transgene in the wing disc squamous epithelium with the *AGiR-GAL4* driver were dissected and fluorescently stained for GFP to increase the signal. GFP and DAPI (included in the mounting medium) were imaged by

performing a z-stack with mosaic acquisition encompassing the whole domain of GFP expression (step size of 0.42 µm). 3D quantitation was performed using Imaris software. Briefly, the volume of the squamous epithelium based on the GFP channel was detected and measured using the surface tool. This volume was then used as a mask on the nuclei image (DAPI staining) to extract nuclei included inside this volume. Those were segmented on the masked DAPI channel with a semi-automatic seeded region growing method, and counted using the surface tool.

***Ex vivo* laser surgery**

Wing discs from late third instar larvae were dissected in Schneider's drosophila medium supplemented with 10% FCS and transferred to 10 wells slides coated with teflon (Fisher 11787394, one disc per well, 30µl of dissection medium per well). Discs were oriented before addition of a coverslip to have the squamous epithelium facing the coverslip. A slit was made in the squamous epithelium using a Zeiss LSM 780 NLO microscope with 40x/1.1W objective. For the ROI-based ablation, the Ti:Sapphire laser was setup at the most efficient wavelength (around 800 nm). Pixel size was setup at 0.2 µm and slit size was 28 µm*0.2 µm. Parameters (Dwell time and Ti:Sapphire power) were established daily on a test disc such that only the squamous epithelium and not the subjacent columnar epithelium was cut (*i.e.* at the limit of cavitation). Time series of 3 pre- and 20 post-ablation acquisitions were done every 500 ms for His2Av-EGFP and transmission images. Tissue deformation was estimated by tracking intracellular granules in the vicinity of the wound on transmission images with ImageJ.

For the quantification, we developed a script in Matlab to align the experiments (based on the ablation ROI extracted from metadata). We projected the deformation on the normalized gradient of wound distance map and then we extracted our deformation data (positive value for dilatation).

ACKNOWLEDGEMENTS

We thank R. Campo Gonzales for help at early stages of this work. We deeply acknowledge S. Pagnotta from the CCMA (Centre Commun de Microscopie Appliquée, Université Nice Sophia Antipolis, Microscopy and Imaging Platform Côte d'Azur, MICA) and M. Mondin and M. Mertz from the PRISM facility (Plateforme PRISM – iBV –CNRS UMR 7277 – Inserm U1091 – Université Côte d'Azur) for excellent technical assistance with, respectively, TEM and fluorescence microscopy. We thank the TRiP at Harvard Medical School (NIH/NIGMS R01-GM084947) for providing transgenic RNAi fly stocks, and the Bloomington Drosophila Stock Center (NIH P40OD018537) and the Vienna Drosophila Resource Center (VDRC, www.vdrc.at) for other fly stocks used in this study. We are indebted to H. Jäckle, A. Holz, R. Momota, F. Besse and the late R. Timple for sharing reagents. We thank N. Parassol-Girard, F. Besse, P. Clary, R. Delanoue and V. Van de Bor for very helpful discussions. We are grateful to C. Médioni and N. Romero for critical reading of the manuscript. Finally, we thank G. Zimniak, and J-B. Coutelis for everlasting support and enthusiasm. S. P. was the recipient of a CNRS-Université Nice Sophia Antipolis "Chaire d'excellence". R. B. held a fellowship from Fondation pour la Recherche Médicale. This work was supported by a grant from the LABEX SIGNALIFE (ANR-11-LABX-0028-01) to P. T.

REFERENCES

1. Shashikanth N, Yeruva S, Ong MLDM, Odenwald MA, Pavlyuk R, Turner JR. Epithelial Organization: The Gut and Beyond. Compr Physiol. 2017;7(4):1497-518. Epub 20170912. doi: 10.1002/cphy.c170003. PubMed PMID: 28915334.
2. Lecuit T, Yap AS. E-cadherin junctions as active mechanical integrators in tissue dynamics. Nat Cell Biol. 2015;17(5):533-9. doi: 10.1038/ncb3136. PubMed PMID: 25925582.
3. Sekiguchi R, Yamada KM. Basement Membranes in Development and Disease. Curr Top Dev Biol. 2018;130:143-91. Epub 2018/03/31. doi: 10.1016/bs.ctdb.2018.02.005. PubMed PMID: 29853176; PubMed Central PMCID: PMCPMC6701859.
4. Yurchenco PD. Integrating Activities of Laminins that Drive Basement Membrane Assembly and Function. Curr Top Membr. 2015;76:1-30. Epub 2015/06/25. doi: 10.1016/bs.ctm.2015.05.001. PubMed PMID: 26610910.
5. Behrens DT, Villone D, Koch M, Brunner G, Sorokin L, Robenek H, et al. The epidermal basement membrane is a composite of separate laminin- or collagen IV-containing networks connected by aggregated perlecan, but not by nidogens. J Biol Chem. 2012;287(22):18700-9. doi: 10.1074/jbc.M111.336073. PubMed PMID: 22493504; PubMed Central PMCID: PMCPMC3365761.
6. Pöschl E, Schlötzer-Schrehardt U, Brachvogel B, Saito K, Ninomiya Y, Mayer U. Collagen IV is essential for basement membrane stability but dispensable for initiation of its assembly during early development. Development. 2004;131(7):1619-28. Epub 2004/03/03. doi: 10.1242/dev.01037. PubMed PMID: 14998921.
7. Urbano JM, Torgler CN, Molnar C, Tepass U, López-Varea A, Brown NH, et al. Drosophila laminins act as key regulators of basement membrane assembly and morphogenesis. Development. 2009;136(24):4165-76. doi: 10.1242/dev.044263. PubMed PMID: 19906841; PubMed Central PMCID: PMCPMC2781052.
8. Wolfstetter G, Dahlitz I, Pfeifer K, Töpfer U, Alt JA, Pfeifer DC, et al. Characterization of *Drosophila Nidogen/entactin* reveals roles in basement membrane stability, barrier function and nervous system patterning. Development. 2019;146(2). Epub 2019/01/16. doi: 10.1242/dev.168948. PubMed PMID: 30567930.
9. Kramer JM. Basement membranes. WormBook. 2005:1-15. Epub 2005/09/01. doi: 10.1895/wormbook.1.16.1. PubMed PMID: 18050423; PubMed Central PMCID: PMCPMC4781274.
10. Jayadev R, Sherwood DR. Basement membranes. Curr Biol. 2017;27(6):R207-R11. doi: 10.1016/j.cub.2017.02.006. PubMed PMID: 28324731.
11. Pastor-Pareja JC, Xu T. Shaping cells and organs in Drosophila by opposing roles of fat body-secreted Collagen IV and perlecan. Dev Cell. 2011;21(2):245-56. doi: 10.1016/j.devcel.2011.06.026. PubMed PMID: 21839919; PubMed Central PMCID: PMCPMC4153364.
12. Haigo SL, Bilder D. Global tissue revolutions in a morphogenetic movement controlling elongation. Science. 2011;331(6020):1071-4. Epub 2011/01/06. doi: 10.1126/science.1199424. PubMed PMID: 21212324; PubMed Central PMCID: PMCPMC3153412.
13. Hollfelder D, Frasch M, Reim I. Distinct functions of the laminin β LN domain and collagen IV during cardiac extracellular matrix formation and stabilization of alary muscle attachments revealed by EMS mutagenesis in Drosophila. BMC Dev Biol. 2014;14:26. Epub

2014/06/17. doi: 10.1186/1471-213X-14-26. PubMed PMID: 24935095; PubMed Central PMCID: PMCPMC4068974.
14. Matsubayashi Y, Louani A, Dragu A, Sánchez-Sánchez BJ, Serna-Morales E, Yolland L, et al. A Moving Source of Matrix Components Is Essential for De Novo Basement Membrane Formation. Curr Biol. 2017;27(22):3526-34.e4. Epub 2017/11/09. doi: 10.1016/j.cub.2017.10.001. PubMed PMID: 29129537; PubMed Central PMCID: PMCPMC5714436.
15. Dai J, Estrada B, Jacobs S, Sánchez-Sánchez BJ, Tang J, Ma M, et al. Dissection of Nidogen function in Drosophila reveals tissue-specific mechanisms of basement membrane assembly. PLoS Genet. 2018;14(9):e1007483. Epub 2018/09/27. doi: 10.1371/journal.pgen.1007483. PubMed PMID: 30260959; PubMed Central PMCID: PMCPMC6177204.
16. Ramos-Lewis W, Page-McCaw A. Basement membrane mechanics shape development: Lessons from the fly. Matrix Biol. 2019;75-76:72-81. Epub 2018/04/12. doi: 10.1016/j.matbio.2018.04.004. PubMed PMID: 29656148; PubMed Central PMCID: PMCPMC6185827.
17. Bonche R, Chessel A, Boisivon S, Smolen P, Thérond P, Pizette S. Two different sources of Perlecan cooperate for its function in the basement membrane of the Drosophila wing imaginal disc. Dev Dyn. 2020. Epub 2020/12/02. doi: 10.1002/dvdy.274. PubMed PMID: 33269518.
18. Crest J, Diz-Muñoz A, Chen DY, Fletcher DA, Bilder D. Organ sculpting by patterned extracellular matrix stiffness. Elife. 2017;6. Epub 2017/06/27. doi: 10.7554/eLife.24958. PubMed PMID: 28653906; PubMed Central PMCID: PMCPMC5503509.
19. Isabella AJ, Horne-Badovinac S. Dynamic regulation of basement membrane protein levels promotes egg chamber elongation in Drosophila. Dev Biol. 2015;406(2):212-21. Epub 2015/09/06. doi: 10.1016/j.ydbio.2015.08.018. PubMed PMID: 26348027; PubMed Central PMCID: PMCPMC4639450.
20. Isabella AJ, Horne-Badovinac S. Rab10-Mediated Secretion Synergizes with Tissue Movement to Build a Polarized Basement Membrane Architecture for Organ Morphogenesis. Dev Cell. 2016;38(1):47-60. doi: 10.1016/j.devcel.2016.06.009. PubMed PMID: 27404358; PubMed Central PMCID: PMCPMC4942852.
21. Chlasta J, Milani P, Runel G, Duteyrat JL, Arias L, Lamiré LA, et al. Variations in basement membrane mechanics are linked to epithelial morphogenesis. Development. 2017;144(23):4350-62. Epub 2017/10/16. doi: 10.1242/dev.152652. PubMed PMID: 29038305.
22. Skeath JB, Wilson BA, Romero SE, Snee MJ, Zhu Y, Lacin H. The extracellular metalloprotease AdamTS-A anchors neural lineages in place within and preserves the architecture of the central nervous system. Development. 2017;144(17):3102-13. Epub 2017/07/31. doi: 10.1242/dev.145854. PubMed PMID: 28760813; PubMed Central PMCID: PMCPMC5611953.
23. Sui L, Pflugfelder GO, Shen J. The Dorsocross T-box transcription factors promote tissue morphogenesis in the Drosophila wing imaginal disc. Development. 2012;139(15):2773-82. doi: 10.1242/dev.079384. PubMed PMID: 22782723.
24. Sui L, Alt S, Weigert M, Dye N, Eaton S, Jug F, et al. Differential lateral and basal tension drive folding of Drosophila wing discs through two distinct mechanisms. Nat Commun. 2018;9(1):4620. Epub 2018/11/05. doi: 10.1038/s41467-018-06497-3. PubMed PMID: 30397306; PubMed Central PMCID: PMCPMC6218478.
25. P.J. B. Pattern formation in imaginal discs. In: T.R.F. AMaW, editor. Biology of Drosophila. 2c. New York: Academic Press; 1978. p. 229-335.

26. Milner MJ, Bleasby AJ, Kelly SL. The role of the peripodial membrane of leg and wing imaginal discs ofDrosophila melanogaster during evagination and differentiation in vitro. Wilehm Roux Arch Dev Biol. 1984;193(3):180-6. doi: 10.1007/BF00848893. PubMed PMID: 28305459.
27. Pastor-Pareja JC, Grawe F, Martín-Blanco E, García-Bellido A. Invasive cell behavior during Drosophila imaginal disc eversion is mediated by the JNK signaling cascade. Dev Cell. 2004;7(3):387-99. doi: 10.1016/j.devcel.2004.07.022. PubMed PMID: 15363413.
28. Gibson MC, Schubiger G. Peripodial cells regulate proliferation and patterning of Drosophila imaginal discs. Cell. 2000;103(2):343-50. doi: 10.1016/s0092-8674(00)00125-2. PubMed PMID: 11057906.
29. Gibson MC, Lehman DA, Schubiger G. Lumenal transmission of decapentaplegic in Drosophila imaginal discs. Dev Cell. 2002;3(3):451-60. doi: 10.1016/s1534-5807(02)00264-2. PubMed PMID: 12361606.
30. Pallavi SK, Shashidhara LS. Egfr/Ras pathway mediates interactions between peripodial and disc proper cells in Drosophila wing discs. Development. 2003;130(20):4931-41. doi: 10.1242/dev.00719. PubMed PMID: 12930782.
31. Nusinow D, Greenberg L, Hatini V. Reciprocal roles for bowl and lines in specifying the peripodial epithelium and the disc proper of the Drosophila wing primordium. Development. 2008;135(18):3031-41. Epub 2008/08/13. doi: 10.1242/dev.020800. PubMed PMID: 18701548; PubMed Central PMCID: PMCPMC2910904.
32. D. F, J.W. F. The metamorphic Development of the Adult Epidermis. In: A. BMaM-A, editor. The development of *Drosophila melanogaster*. II. New York: Cold Spring Harbor Laboratory Press; 1993. p. 843-97.
33. Srivastava A, Pastor-Pareja JC, Igaki T, Pagliarini R, Xu T. Basement membrane remodeling is essential for Drosophila disc eversion and tumor invasion. Proc Natl Acad Sci U S A. 2007;104(8):2721-6. doi: 10.1073/pnas.0611666104. PubMed PMID: 17301221; PubMed Central PMCID: PMCPMC1815248.
34. Aldaz S, Escudero LM, Freeman M. Dual role of myosin II during Drosophila imaginal disc metamorphosis. Nat Commun. 2013;4:1761. doi: 10.1038/ncomms2763. PubMed PMID: 23612302; PubMed Central PMCID: PMCPMC3736102.
35. Voigt A, Pflanz R, Schäfer U, Jäckle H. Perlecan participates in proliferation activation of quiescent Drosophila neuroblasts. Dev Dyn. 2002;224(4):403-12. doi: 10.1002/dvdy.10120. PubMed PMID: 12203732.
36. Zang Y, Wan M, Liu M, Ke H, Ma S, Liu LP, et al. Plasma membrane overgrowth causes fibrotic collagen accumulation and immune activation in Drosophila adipocytes. Elife. 2015;4:e07187. Epub 2015/06/19. doi: 10.7554/eLife.07187. PubMed PMID: 26090908; PubMed Central PMCID: PMCPMC4490375.
37. Friedrich MV, Schneider M, Timpl R, Baumgartner S. Perlecan domain V of Drosophila melanogaster. Sequence, recombinant analysis and tissue expression. Eur J Biochem. 2000;267(11):3149-59. PubMed PMID: 10824099.
38. Schneider M, Khalil AA, Poulton J, Castillejo-Lopez C, Egger-Adam D, Wodarz A, et al. Perlecan and Dystroglycan act at the basal side of the Drosophila follicular epithelium to maintain epithelial organization. Development. 2006;133(19):3805-15. doi: 10.1242/dev.02549. PubMed PMID: 16943280; PubMed Central PMCID: PMCPMC2753471.
39. You J, Zhang Y, Li Z, Lou Z, Jin L, Lin X. Drosophila perlecan regulates intestinal stem cell activity via cell-matrix attachment. Stem Cell Reports. 2014;2(6):761-9. doi: 10.1016/j.stemcr.2014.04.007. PubMed PMID: 24936464; PubMed Central PMCID: PMCPMC4050351.

40. Sher I, Zisman-Rozen S, Eliahu L, Whitelock JM, Maas-Szabowski N, Yamada Y, et al. Targeting perlecan in human keratinocytes reveals novel roles for perlecan in epidermal formation. J Biol Chem. 2006;281(8):5178-87. doi: 10.1074/jbc.M509500200. PubMed PMID: 16269412.
41. Datta S. Control of proliferation activation in quiescent neuroblasts of the Drosophila central nervous system. Development. 1995;121(4):1173-82. PubMed PMID: 7743929.
42. Milán M, Campuzano S, García-Bellido A. Developmental parameters of cell death in the wing disc of Drosophila. Proc Natl Acad Sci U S A. 1997;94(11):5691-6. doi: 10.1073/pnas.94.11.5691. PubMed PMID: 9159134; PubMed Central PMCID: PMCPMC20840.
43. McClure KD, Schubiger G. Developmental analysis and squamous morphogenesis of the peripodial epithelium in Drosophila imaginal discs. Development. 2005;132(22):5033-42. doi: 10.1242/dev.02092. PubMed PMID: 16236766.
44. Sedlak BJ, Manzo R, Stevens M. Localized cell death in Drosophila imaginal wing disc epithelium caused by the mutation apterous-blot. Dev Biol. 1984;104(2):489-96. doi: 10.1016/0012-1606(84)90106-4. PubMed PMID: 6430736.
45. Bhave G, Colon S, Ferrell N. The sulfilimine cross-link of collagen IV contributes to kidney tubular basement membrane stiffness. Am J Physiol Renal Physiol. 2017;313(3):F596-F602. Epub 2017/04/19. doi: 10.1152/ajprenal.00096.2017. PubMed PMID: 28424209; PubMed Central PMCID: PMCPMC5625101.
46. Wang X, Harris RE, Bayston LJ, Ashe HL. Type IV collagens regulate BMP signalling in Drosophila. Nature. 2008;455(7209):72-7. doi: 10.1038/nature07214. PubMed PMID: 18701888.
47. Baena-López LA, Pastor-Pareja JC, Resino J. Wg and Egfr signalling antagonise the development of the peripodial epithelium in Drosophila wing discs. Development. 2003;130(26):6497-506. doi: 10.1242/dev.00884. PubMed PMID: 14660540.
48. Costell M, Gustafsson E, Aszódi A, Mörgelin M, Bloch W, Hunziker E, et al. Perlecan maintains the integrity of cartilage and some basement membranes. J Cell Biol. 1999;147(5):1109-22. PubMed PMID: 10579729; PubMed Central PMCID: PMCPMC2169352.
49. Rossi M, Morita H, Sormunen R, Airenne S, Kreivi M, Wang L, et al. Heparan sulfate chains of perlecan are indispensable in the lens capsule but not in the kidney. EMBO J. 2003;22(2):236-45. doi: 10.1093/emboj/cdg019. PubMed PMID: 12514129; PubMed Central PMCID: PMCPMC140094.
50. Morita H, Yoshimura A, Inui K, Ideura T, Watanabe H, Wang L, et al. Heparan sulfate of perlecan is involved in glomerular filtration. J Am Soc Nephrol. 2005;16(6):1703-10. doi: 10.1681/ASN.2004050387. PubMed PMID: 15872080.
51. Inomata T, Ebihara N, Funaki T, Matsuda A, Watanabe Y, Ning L, et al. Perlecan-deficient mutation impairs corneal epithelial structure. Invest Ophthalmol Vis Sci. 2012;53(3):1277-84. Epub 2012/03/09. doi: 10.1167/iovs.11-8742. PubMed PMID: 22266517.
52. Celestrin K, Díaz-Balzac CA, Tang LTH, Ackley BD, Bülow HE. Four specific immunoglobulin domains in UNC-52/Perlecan function with NID-1/Nidogen during dendrite morphogenesis in Caenorhabditis elegans. Development. 2018;145(10). Epub 2018/05/14. doi: 10.1242/dev.158881. PubMed PMID: 29678816; PubMed Central PMCID: PMCPMC6001381.
53. Grigorian M, Liu T, Banerjee U, Hartenstein V. The proteoglycan Trol controls the architecture of the extracellular matrix and balances proliferation and differentiation of blood progenitors in the Drosophila lymph gland. Dev Biol. 2013;384(2):301-12. doi: 10.1016/j.ydbio.2013.03.007. PubMed PMID: 23510717; PubMed Central PMCID: PMCPMC4278754.

54. Ramos-Lewis W, LaFever KS, Page-McCaw A. A scar-like lesion is apparent in basement membrane after wound repair in vivo. Matrix Biol. 2018;74:101-20. Epub 2018/07/05. doi: 10.1016/j.matbio.2018.07.004. PubMed PMID: 29981372; PubMed Central PMCID: PMCPMC6250587.
55. Jayadev R, Chi Q, Keeley DP, Hastie EL, Kelley LC, Sherwood DR. α-Integrins dictate distinct modes of type IV collagen recruitment to basement membranes. J Cell Biol. 2019;218(9):3098-116. Epub 2019/08/06. doi: 10.1083/jcb.201903124. PubMed PMID: 31387941; PubMed Central PMCID: PMCPMC6719451.
56. Farach-Carson MC, Warren CR, Harrington DA, Carson DD. Border patrol: insights into the unique role of perlecan/heparan sulfate proteoglycan 2 at cell and tissue borders. Matrix Biol. 2014;34:64-79. doi: 10.1016/j.matbio.2013.08.004. PubMed PMID: 24001398; PubMed Central PMCID: PMCPMC3938997.
57. Brown KL, Cummings CF, Vanacore RM, Hudson BG. Building collagen IV smart scaffolds on the outside of cells. Protein Sci. 2017;26(11):2151-61. doi: 10.1002/pro.3283. PubMed PMID: 28845540; PubMed Central PMCID: PMCPMC5654846.
58. Yurchenco PD, Ruben GC. Basement membrane structure in situ: evidence for lateral associations in the type IV collagen network. J Cell Biol. 1987;105(6 Pt 1):2559-68. doi: 10.1083/jcb.105.6.2559. PubMed PMID: 3693393; PubMed Central PMCID: PMCPMC2114722.
59. Okada M, Imoto K, Sugiyama A, Yasuda J, Yamawaki H. New Insights into the Role of Basement Membrane-Derived Matricryptins in the Heart. Biol Pharm Bull. 2017;40(12):2050-60. doi: 10.1248/bpb.b17-00308. PubMed PMID: 29199230.
60. Aumailley M, Wiedemann H, Mann K, Timpl R. Binding of nidogen and the laminin-nidogen complex to basement membrane collagen type IV. Eur J Biochem. 1989;184(1):241-8. doi: 10.1111/j.1432-1033.1989.tb15013.x. PubMed PMID: 2506015.
61. Resino J, Salama-Cohen P, García-Bellido A. Determining the role of patterned cell proliferation in the shape and size of the Drosophila wing. Proc Natl Acad Sci U S A. 2002;99(11):7502-7. doi: 10.1073/pnas.072208199. PubMed PMID: 12032312; PubMed Central PMCID: PMCPMC124260.
62. Kvist AJ, Johnson AE, Mörgelin M, Gustafsson E, Bengtsson E, Lindblom K, et al. Chondroitin sulfate perlecan enhances collagen fibril formation. Implications for perlecan chondrodysplasias. J Biol Chem. 2006;281(44):33127-39. doi: 10.1074/jbc.M607892200. PubMed PMID: 16956876.
63. Arikawa-Hirasawa E, Rossi SG, Rotundo RL, Yamada Y. Absence of acetylcholinesterase at the neuromuscular junctions of perlecan-null mice. Nat Neurosci. 2002;5(2):119-23. doi: 10.1038/nn801. PubMed PMID: 11802174.
64. Balasubramani M, Schreiber EM, Candiello J, Balasubramani GK, Kurtz J, Halfter W. Molecular interactions in the retinal basement membrane system: a proteomic approach. Matrix Biol. 2010;29(6):471-83. Epub 2010/04/18. doi: 10.1016/j.matbio.2010.04.002. PubMed PMID: 20403434.
65. Battaglia C, Mayer U, Aumailley M, Timpl R. Basement-membrane heparan sulfate proteoglycan binds to laminin by its heparan sulfate chains and to nidogen by sites in the protein core. Eur J Biochem. 1992;208(2):359-66. doi: 10.1111/j.1432-1033.1992.tb17195.x. PubMed PMID: 1521532.
66. Heljasvaara R, Aikio M, Ruotsalainen H, Pihlajaniemi T. Collagen XVIII in tissue homeostasis and dysregulation - Lessons learned from model organisms and human patients.

Matrix Biol. 2017;57-58:55-75. Epub 2016/10/13. doi: 10.1016/j.matbio.2016.10.002. PubMed PMID: 27746220.
67. Arikawa-Hirasawa E, Watanabe H, Takami H, Hassell JR, Yamada Y. Perlecan is essential for cartilage and cephalic development. Nat Genet. 1999;23(3):354-8. doi: 10.1038/15537. PubMed PMID: 10545953.
68. Mirouse V, Christoforou CP, Fritsch C, St Johnston D, Ray RP. Dystroglycan and perlecan provide a basal cue required for epithelial polarity during energetic stress. Dev Cell. 2009;16(1):83-92. doi: 10.1016/j.devcel.2008.11.006. PubMed PMID: 19154720; PubMed Central PMCID: PMCPMC2789236.
69. Haack T, Bergstralh DT, St Johnston D. Damage to the Drosophila follicle cell epithelium produces "false clones" with apparent polarity phenotypes. Biol Open. 2013;2(12):1313-20. Epub 2013/12/15. doi: 10.1242/bio.20134671. PubMed PMID: 24337115; PubMed Central PMCID: PMCPMC3863415.
70. Herranz H, Weng R, Cohen SM. Crosstalk between epithelial and mesenchymal tissues in tumorigenesis and imaginal disc development. Curr Biol. 2014;24(13):1476-84. doi: 10.1016/j.cub.2014.05.043. PubMed PMID: 24980505.
71. Spencer AK, Siddiqui BA, Thomas JH. Cell shape change and invagination of the cephalic furrow involves reorganization of F-actin. Dev Biol. 2015;402(2):192-207. Epub 2015/04/28. doi: 10.1016/j.ydbio.2015.03.022. PubMed PMID: 25929228.
72. Dasgupta A, Merkel M, Clark MJ, Jacob AE, Dawson JE, Manning ML, et al. Cell volume changes contribute to epithelial morphogenesis in zebrafish Kupffer's vesicle. Elife. 2018;7. Epub 2018/01/29. doi: 10.7554/eLife.30963. PubMed PMID: 29376824; PubMed Central PMCID: PMCPMC5800858.
73. Ma M, Cao X, Dai J, Pastor-Pareja JC. Basement Membrane Manipulation in Drosophila Wing Discs Affects Dpp Retention but Not Growth Mechanoregulation. Dev Cell. 2017;42(1):97-106.e4. doi: 10.1016/j.devcel.2017.06.004. PubMed PMID: 28697337.
74. Saias L, Swoger J, D'Angelo A, Hayes P, Colombelli J, Sharpe J, et al. Decrease in Cell Volume Generates Contractile Forces Driving Dorsal Closure. Dev Cell. 2015;33(5):611-21. Epub 2015/05/14. doi: 10.1016/j.devcel.2015.03.016. PubMed PMID: 25982674.
75. Monier B, Gettings M, Gay G, Mangeat T, Schott S, Guarner A, et al. Apico-basal forces exerted by apoptotic cells drive epithelium folding. Nature. 2015;518(7538):245-8. Epub 2015/01/21. doi: 10.1038/nature14152. PubMed PMID: 25607361.
76. Hayes P, Solon J. Drosophila dorsal closure: An orchestra of forces to zip shut the embryo. Mech Dev. 2017;144(Pt A):2-10. Epub 2017/01/07. doi: 10.1016/j.mod.2016.12.005. PubMed PMID: 28077304.
77. Kashgari G, Meinecke L, Gordon W, Ruiz B, Yang J, Ma AL, et al. Epithelial Migration and Non-adhesive Periderm Are Required for Digit Separation during Mammalian Development. Dev Cell. 2020;52(6):764-78.e4. Epub 2020/02/27. doi: 10.1016/j.devcel.2020.01.032. PubMed PMID: 32109382; PubMed Central PMCID: PMCPMC8237330.
78. Morin X, Daneman R, Zavortink M, Chia W. A protein trap strategy to detect GFP-tagged proteins expressed from their endogenous loci in Drosophila. Proc Natl Acad Sci U S A. 2001;98(26):15050-5. Epub 2001/12/14. doi: 10.1073/pnas.261408198. PubMed PMID: 11742088; PubMed Central PMCID: PMCPMC64981.
79. Pirrotta V, editor. *Drosophila*: A practical approach. Oxford: IRL Press; 1986.
80. Lehner CF, O'Farrell PH. The Roles of Drosophila Cyclins A and B in Mitotic Control. Cell. 1990;61(3):535-47. PubMed PMID: 2139805; PubMed Central PMCID: PMC2753431.

81. Wolfstetter G, Shirinian M, Stute C, Grabbe C, Hummel T, Baumgartner S, et al. Fusion of circular and longitudinal muscles in Drosophila is independent of the endoderm but further visceral muscle differentiation requires a close contact between mesoderm and endoderm. Mech Dev. 2009;126(8-9):721-36. Epub 2009/05/26. doi: 10.1016/j.mod.2009.05.001. PubMed PMID: 19463947.
82. Momota R, Naito I, Ninomiya Y, Ohtsuka A. Drosophila type XV/XVIII collagen, Mp, is involved in Wingless distribution. Matrix Biol. 2011;30(4):258-66. doi: 10.1016/j.matbio.2011.03.008. PubMed PMID: 21477650.
83. Robb JA. Maintenance of imaginal discs of Drosophila melanogaster in chemically defined media. J Cell Biol. 1969;41(3):876-85. Epub 1969/06/01. PubMed PMID: 5768877; PubMed Central PMCID: PMCPMC2107816.
84. Aigouy B, Umetsu D, Eaton S. Segmentation and Quantitative Analysis of Epithelial Tissues. Methods Mol Biol. 2016;1478:227-39. doi: 10.1007/978-1-4939-6371-3_13. PubMed PMID: 27730585.
85. Heller D, Hoppe A, Restrepo S, Gatti L, Tournier AL, Tapon N, et al. EpiTools: An Open-Source Image Analysis Toolkit for Quantifying Epithelial Growth Dynamics. Dev Cell. 2016;36(1):103-16. doi: 10.1016/j.devcel.2015.12.012. PubMed PMID: 26766446; PubMed Central PMCID: PMCPMC4712040.

FIGURE LEGENDS

Figure 1: **A new mutation in *trol* affects morphogenesis of the adult wing and the three epithelia of the wing disc**

(**A-C**) Bright-field images of late pupae (**A,B**) or an adult fly (**C**) of the indicated genotype. (**A**) In wild-type (*wt*) pupae, the right (R) and left (L) wings (darkly pigmented tissue) are both seen through the ventral side of the pupal case. (**B**) In the *trol* mutant pupa (*JO271#49*), the right wing is normally positioned on the ventral side, whereas the left one is bent backwards and can only be seen through the dorsal side of the pupal case. (**C**) Depicts an incomplete eversion phenotype whereby an adult *trol* mutant fly still has the distal part of its right wing inside its body (arrow).

(**D**) Confocal images of transverse sections parallel to the anterior/posterior axis of late third instar wing discs (dashed line in **E** illustrates the plane of section) of the indicated genotype, labeled by immunofluorescence for Trol (green) and F-actin (red). Anterior is to the right, and the squamous epithelium and the apical side of columnar cells are up. Scale bar (20 μm) is shown on the wild-type (*wt*). In the *trol* mutant (*JO271#49*), the columnar epithelium is taller (white bar, same size as the one on the *wt*), and sometimes ectopically folded on the apical side (arrowhead). In addition, the folds of the lateral anterior cuboidal epithelium (numbered 1 to 3) are abnormally packed, the lateral posterior cuboidal epithelium exhibits ectopic folds (asterisks), and the region where cells are squamous is reduced (delimited by the arrows).

(**E**) Confocal images of late third instar wing discs of the indicated genotype, and expressing a cytoplasmic GFP (green) under the control of *AGiRGAL4* to label the squamous epithelium, confirm that the surface area of this epithelium is drastically reduced in the *trol* mutant (*JO271#49*). Anterior is to the right and dorsal is up. Scale bar (20 μm) is shown on the wild-type (*wt*).

Figure 2: **Trol is necessary for the flattening of the SE's cells**

(**A,A'**) View from the basal side of an Imaris 3D reconstitution of the squamous epithelium of late third instar wing discs. The volume of the tissue is based on the expression of a cytoplasmic GFP under the control of *AGiRGAL4* in the indicated genotypes (**A**). Nuclei were then segmented within this volume (**A'**). Anterior is to the right and dorsal is up. Scale bar (100 μm) is shown in (**A**).

(**B**) Quantification of the squamous epithelium volume, nuclei number and density. Datasets are represented by box-and-whisker plots. Horizontal lines are medians and box hinges are 25th and

75th percentiles. Whiskers indicate 5th and 95th percentiles. Non-parametric statistics and plots were obtained with the GraphPad Prism software. Comparisons with the Wilcoxon test show that in the *trol* mutant (*trol*$^{JO271\#49}$: *JO271#49*), while the cell number of the tissue (witnessed by the nuclei number) is not significantly different, its volume is reduced and this is accompanied by a rise in cell density. (*wt*: N=9, *JO271#49:* N=15, ****: p<0.0001, NS: not significant).

(**C**) Close-ups of the confocal longitudinal sections parallel to the dorsal/ventral axis shown in Fig 6A''',B'''. Discs from the indicated genotypes were labeled by immunofluorescence for Ndg (green) and stained with DAPI to highlight nuclei (red) and with phalloidin to reveal F-actin (blue, or white when shown alone). The squamous epithelium is to the left and dorsal is up. The squamous epithelium (bordered by arrows) of the *trol*$^{JO271\#49}$ mutant (*JO271#49)* is thicker than that of the control (*wt*) and its cells have a cuboidal morphology.

(**D,D'**) Confocal images of the squamous epithelium (**D**) and of transverse sections parallel to the anterior/posterior axis (**D'**, plane of section shown by the white dashed line in **D**) of late third instar wing discs of the indicated genotype, stained with DAPI to highlight nuclei and F-actin to depict cell shape. (**D**) Anterior is to the right and dorsal is up. (**D'**) Anterior is to the right and the squamous epithelium, which is delimited by arrows, is up. Scale bar (20 μm) for (**D,D'**) is shown in (**D**). Ubiquitous depletion of *trol* with the *UAS-trol.RNAi*^{JF03376} and *UAS-Dcr-2 (RNAi trol)* expressed with *ActinGAL4 (ActG4*), results in the loss of squamous cell morphology, as seen by the absence of spaced (**D**) and flat nuclei (DAPI in **D'**), and the appearance of cuboidal-like shaped cells (F-actin in **D'**). Furthermore, the wing disc is extremely compacted along the anterior/posterior axis (**D'**), and in the lateral cuboidal epithelium, there is ectopic folding on the posterior side (asterisks) and cramming of the folds (numbered 1 to 3) of the anterior side.

(**E**) TEM micrographs of transverse ultra-thin sections parallel to the anterior/posterior axis (plane of section shown by the white dashed line in **D**) of a late third instar wing disc of the indicated genotype. Top image shows the entire tissue, scale bar (50 μm) is indicated on the micrograph. Bottom image is an enlargement of the region boxed in yellow on the top image, scale bar (10 μm) is indicated on the micrograph. Anterior is to the right and the region where the squamous epithelium should be is up. Bottom image: The ubiquitous depletion of *trol* converts squamous cells into cuboidal ones (see morphology of the cells on either side of the red dashed line), and the former squamous epithelium becomes bi-layered in some regions (the red dashed line is drawn in between the two layers) and invades the lumen of the wing disc (delimited by blue dotted line).

Figure 3: **Trol is required for proper ultrastructure of the SE BM and the incorporation and/or maintenance of Collagen IV and Nidogen**

(**A**) TEM micrographs of transverse ultra-thin sections parallel to the anterior/posterior axis of control (*wt*, left column) or *trol* mutant (*JO271#49*, right column) late third instar wing discs. (**Top**) Images showing the entire tissue and the location of the regions magnified in the middle and bottom images. Scale bar (50 μm) is indicated on the micrograph for the *wt*. (**Middle, bottom**) Images showing the BM of the squamous epithelium. Scale bar (500 nm) is indicated on the micrograph for the *wt* (left). For all images, anterior is to the right and the squamous epithelium is up. The red brackets delineate the BM, and the arrow in the *trol* mutant points to a region consisting of the hairy outer layer only (see text for details).

(**B**) Quantification of the squamous epithelium (SE) BM thickness. The dataset is represented by box-and-whisker plots. Horizontal lines are medians and box hinges are 25^{th} and 75^{th} percentiles. Whiskers indicate 5^{th} and 95^{th} percentiles. Non-parametric statistics and plots were obtained with the GraphPad Prism software. Comparison with the Wilcoxon test shows a significant decrease of the BM thickness in the *trol* mutant (wt: N=60, *JO271#49*: N=60, ****: $p<0.0001$).

(**C-G**) Confocal longitudinal sections parallel to the dorsal/ventral axis (**C-E**, plane of section shown by the white dashed line in **F**) and confocal images of xyz section of the squamous epithelium (**F,G**) of late third instar wing discs of the indicated genotype, labeled by immunofluorescence for Laminin (Lam, green in **C,F**), or Nidogen (Ndg, green in **D,** red in **G**), or directly visualized for Viking-GFP, a protein trap of one of the two alpha chains of Collagen IV (Vkg, green in **E,G**). (**C-E)** The squamous epithelium is to the left and dorsal is up. Scale bar (20 μm) is indicated in (**C)** on the separate channel for Lam. Lam, Ndg and Vkg are still deposited around the wing disc in the *trol* mutant ($trol^{JO271\#49}$), however the folding of the cuboidal epithelium of the ventral pleura is abnormal (folds are numbered from 1 to 4), and for the pouch columnar epithelium, apical ectopic folding and basal detachment from the BM are sometimes seen (arrowhead and arrows, respectively). (**F,G**) Anterior is to the right and dorsal is up. Scale bars (20 μm) are indicated in (**F)** on the separate channel for Lam, and in (**G**) on the separate channel for Vkg. In the absence of Trol ($trol^{JO271\#49}$), Lam distribution is normal in the squamous epithelium BM, whereas the distribution of Ndg and Vkg is altered, as overlapping fibril-like structures parallel to the anterior/posterior axis are visible in, respectively, negative or positive (arrows).

Note that in (**F,G**) the apparent pattern seen with the staining for the BM components at the level of the squamous epithelium in *wt* specimens is an artefact. The staining actually reveals a uniform layer but as the tissue is not stretched (see Fig **2A**) and the image acquisition corresponds to a single confocal plane, it appears as if the staining outlines cells. Conversely, the fibril-like structures observed for Ndg and Vkg are real and do not reflect folds in the squamous epithelium, as the tissue is stretched (Fig **2A**).

Figure 4: **Trol controls the mechanical properties of the SE**

(A-B') Assessment of squamous epithelium (SE) mechanical stress along the anterior/posterior (A/P) axis. The central region of the SE (boxed on the wing disc scheme in **A**) of wild-type (*wt*, image shown in **A** as an example) and *trol* mutant *(J0271#49*) wing discs expressing His2AV-EGFP reporter, were slit along the D/V axis (pink line in **A-B'**), and the consecutive relaxation of the tissue was quantified by tracking intracellular granules visible in transmitted light (white arrowheads on the image in **A**). The D/V slit allowed the analysis of the mechanical stress along the A/P axis. Granules movements are represented by colored vectors in (**B,B'**) and each color corresponds to granules tracked from a single wing disc. Anterior is to the right and dorsal is up.

(C,C') relaxation values were obtained by averaging the distances covered by the granules from the wound between different wing discs (**C**). The dataset is represented by box-and-whisker plots. Horizontal lines are medians and box hinges are 25th and 75th percentiles. Whiskers indicate 5th and 95th percentiles. Comparison with the Wilcoxon test shows a statistically significant increase in the relaxation of the SE upon the D/V slit in the *trol* mutant (*wt*: N=6 wing discs in which the relaxation was null, *J0271#49*: N=16 wing discs, *: $p<0.05$). Vectors resulting from the movement of each granule were decomposed into two vectors, one parallel to the laser slit, and the other perpendicular, and their length was plotted to assess, respectively, the parallel and the perpendicular deformation of the tissue (**C'**). The dataset is represented by box-and-whisker plots. Horizontal lines are medians and box hinges are 25th and 75th percentiles. Whiskers indicate 5th and 95th percentiles. Comparison with the Wilcoxon test shows a strong bias in the *trol* mutant toward perpendicular deformation of the SE following the D/V slit (*wt*: N=364 granules, *J0271#49*: N=560 granules, ****: $p<0.0001$). Non-parametric statistics and plots were obtained with the GraphPad Prism software.

Figure 5: **Decreasing Col IV in the *trol* mutant rescues morphogenesis of the squamous epithelium of the wing disc and the adult wing**

(**A-B'''**) Confocal images of late third instar wing discs of the indicated genotype, taken at the level of the squamous epithelium (**A,B**), at the very basal side of the columnar epithelium (**A',B'**), or corresponding to transverse sections parallel to the anterior/posterior axis (**A'',B"**, dashed line in **A** shows plane of section) and to longitudinal sections parallel to the dorsal/ventral axis (**A''',B'''**, dashed line in **A'** shows plane of section). The tissue is stained with DAPI to highlight nuclei (red, or white when shown alone) and with phalloidin to reveal F-actin (blue, or white when shown alone). (**A-B'**) Anterior is to the right and dorsal is up. (**A'',B''**) Anterior is to the right and the squamous epithelium is up. (**A''',B'''**) The squamous epithelium is to the left and dorsal is up. Scale bars (20 μm) are shown in (**A**) on the separate channel for DAPI for xyz sections, and in (**A''**) on the separate channel for F-actin for all xzy sections.

(**A-B'''**) The introduction of one copy of a mutant allele for *Viking* ($Vkg^{+/-}$) in the *trol* mutant context (*JO271#49*) increases the spreading of the squamous cells as seen by the distance between their nuclei (DAPI, compare **A** and **B**, region encompassed by the double-sided arrows) and the surface they span (F-actin, delimited by arrows in **A'',B''**), but the surface of the basal columnar epithelium is not significantly expanded (compare **A'** and **B'**, double-sided arrows). However, the folds of the lateral anterior cuboidal epithelium (numbered 1 to 3 in **A'',B''**) and of the ventral pleura cuboidal epithelium (numbered 1 to 4 in **A''',B'''**) are more relaxed, and the lateral posterior cuboidal epithelium is no longer ectopically folded (asterisk in **A''**).

(**C**) Quantification of the width of the squamous epithelium (SE) and of the basal width of the wing disc (pouch) along the double-sided arrows shown in (**A,B**) and (**A',B'**), respectively. Datasets are represented by box-and-whisker plots. Horizontal lines are medians and box hinges are 25th and 75th percentiles. Whiskers indicate 5th and 95th percentiles. Comparisons with the Wilcoxon rank sum test were used (****: $p<0.0001$, NS: not significant). $trol^{JO271\#49}$ (*JO*): N=11, $trol^{JO271\#49}$ $Vkg^{+/-}$ (*JO* $Vkg^{+/-}$): N=9. Non-parametric statistics and plots were obtained with the R software.

(**D**) **Left graph**: In control conditions ($Vkg^{+/+}$, N=730), the rate of eclosion of *trol* mutant flies ($trol^{JO271\#49}$: *JO*) is 21.6%. This is brought to 60.8 % upon introduction of one copy of the *Vkg* mutant allele in the genetic background ($Vkg^{+/-}$, N=897), indicating a partial rescue of the lethality. Data were collected from 3 independent experiments.

Right graph: Distribution of wing phenotypes among the population of *trol* mutant adult flies carrying or not one copy of the *Vkg* mutant allele and collected from the experiment shown on the left graph (*JO,* N=79 and *JO Vkg*$^{+/-}$, N=238, respectively). In the *trol* mutant alone, 77.2 % of wings are wild-type (wt, green), 16.4% are misshapen (grey) and 6.3% have eversion defects (black). The decrease in Col IV leads to a strong rescue of the wing phenotypes as 98.3% of wings are wt, 1.7% are misshapen and none show an eversion defect.

Figure 6: **The defective SE's morphogenesis of the *trol* mutant triggers overall defective wing disc architecture**

(**A-C'''**) Confocal images of late third instar wing discs of the indicated genotype, taken at the level of the squamous epithelium (**A,B,C**), or at the very basal side of the columnar epithelium (**A',B',C'**), or corresponding to transverse sections parallel to the anterior/posterior axis (**A'',B",C''**, dashed line in **A** shows plane of section) or to longitudinal sections parallel to the dorsal/ventral axis (**A''',B''',C'''**, dashed line in **A'** shows plane of section). (**A-C'**) Anterior is to the right and dorsal is up. (**A''-C''**) Anterior is to the right and the squamous epithelium is up. (**A'''-C'''**) The squamous epithelium is to the left and dorsal is up. Scale bars (20 μm) are shown in (**A**) for all xyz sections and in (**A''**) and (**A'''**) for xzy sections.

(**A-C'''**) The tissue is labeled by immunofluorescence for Ndg (green, or white when shown alone) and stained with DAPI to highlight nuclei (red, or white when shown alone) and with phalloidin to reveal F-actin (blue, or white when shown alone). (**A,A',A'',A'''**) control sample (*wt*). (**B,B',B'',B'''**) *trol* mutant (*trol*$^{JO271\#49}$: *JO*). (**C,C',C'',C'''**) *trol* mutant with expression of the MMP2 collagenase in the wing disc squamous epithelium restricted to the late third instar stage using *CoroGAL4* (*JO MMP*). The expression of MMP in the *trol* mutant disrupts the squamous epithelium BM but not the cuboidal and columnar BMs, as seen with Ndg staining (**A-C** and **A'-C'**, respectively). This leads to an increased spacing of the nuclei of the squamous cells together with a rupture of this epithelium (**A-C,** DAPI, region encompassed by the double-sided arrows), and to a restoration of the surface area covered by these cells (delimited by arrows in **A''-C''**, F-actin). Strikingly, the basal surface of the columnar epithelium is also widened (**A'-C'**, DAPI, double-sided arrows), and the folds of the lateral anterior and ventral pleura cuboidal epithelium are less compacted (**A''-C"**, numbered 1 to 3, F-actin, and **A'''-C'''**, numbered 1 to 4, F-actin,

respectively). Ectopic folding of the lateral posterior cuboidal epithelium, however, is still observed (**A''-C''**, F-actin, asterisks).

(**D**) Quantification of the width of the squamous epithelium (SE) and of the basal width of the wing disc (pouch) along the double-sided arrows shown in (**A,B,C**) and (**A',B',C'**), respectively. Datasets are represented by box-and-whisker plots. Horizontal lines are medians and box hinges are 25th and 75th percentiles. Whiskers indicate 5th and 95th percentiles and black dots are values beyond these limits. Pairwise comparisons with the Wilcoxon rank sum test and Benjamini-Hochberg correction were used (**: $p<0.01$, NS: not significant). *wt*: N=7, *JO*: N=7, *JO MMP*: N=6. Non-parametric statistics and plots were obtained with the R software.

Figure S1: **The *trol*$^{JO271\#49}$ mutation leads to a general reduction in *trol* RNA and protein**

(**A**) Scheme of the wing disc illustrating the three different epithelia of this tissue and the position of its BM. (**Left**) En face view from the squamous epithelium (SE) side with the columnar epithelium (CoE) laying underneath, anterior is to the right and dorsal is up. (**Middle, Top**) Longitudinal section parallel to the dorsal/ventral axis (*i.e.*, parallel to the anterior/posterior boundary, straight pink dashed line on the left image), the SE is to the left and dorsal is up. (**Middle, Bottom**) Longitudinal section parallel to the anterior/posterior axis (*i.e.*, parallel to the dorsal/ventral boundary, green dashed line on the left image), anterior is to the right and the SE is up. The different regions of the CoE and the cuboidal epithelium (CuE) are indicated by letters. N: notum, H: hinge, P: pouch, VP: ventral pleura, PLP: posterior lateral pleura, ALP: anterior lateral pleura. Note that for the different types of views, the same orientation will be kept throughout the figures.

(**B**) Genomic representation of the *trol* locus with exons relevant to this study (rectangles, numbering according to Flybase). For simplicity, long introns are not shown to scale and 3' exons are omitted, except for the last one, exon 56. Non-represented intervening sequences are indicated by slashes. The black arrowhead indicates the location of the P-element (G0271) that was jumped out, generating the deletion found in the *trol* mutant allele *trol*$^{JO271\#49}$ (black bracket). Arrows show the position of the pair of primers used in (**C**).

(**C**) RT-qPCR on RNA extracted from late third instar larvae of the indicated genotype. Primers for exons 35 and 36, predicted to be common to all *trol* isoforms, were used. Average values plus

and minus SEM are shown. The *trol*$^{JO271\#49}$ mutant allele leads to a strong downregulation of *trol* RNA.

(**D,E**) Bright field images of late third instar wing discs (**D**) and fat bodies (**E**) of the indicated genotypes, processed for RNA *in situ* hybridization with a *trol* probe against exon 36. (**D**) Anterior is to the right and dorsal is up, scale bar (20 μm) is indicated on the picture of the control (*wt*). Asterisks point to adepithelial cells associated to the notum region, and the pouch is circumscribed by a circle. (**E**) Scale bar (40 μm) is indicated on the picture of the *wt*. The salivary gland (SG) is outlined by the black dotted line and does not express *trol*, providing a control for background staining. *trol* mRNA is strongly reduced in the *trol* mutant (*trol*$^{JO271\#49}$), both in the wing disc (**D**) and in the fat body (**E**).

(**F**) Confocal images of late third instar fat bodies and wing discs of the indicated genotype, labeled by immunofluorescence for Trol (white). For discs, anterior is to the right and dorsal is up. Scale bars (20 μm) are shown on the images of the *wt* fat body and the *wt* wing disc SE. In the *trol* mutant, Trol protein is mostly absent from the BM of the wing disc SE and pouch columnar epithelium (CoE), but some protein is still detected at the level of the cuboidal epithelium (CuE), as well as between fat body cells (circles) an their BM (arrows). In the wing disc, arrowheads point to the adepithelial cells, and the asterisks, to remnants of Trol expression in the mutant condition.

Figure S2: **Epithelial cells of the wing disc retain normal apico-basal polarity in the absence of Trol**

(**A-D"**) Confocal images of longitudinal sections parallel to the dorsal/ventral axis of late third instar wing discs of the indicated genotype, labeled by immunofluorescence for PKCζ (Pkc, green) and DE-cadherin (Cad, red) (**A-B''**), or Cad (red) and Disc large (Dlg, green) (**C-D''**). Enlargements in (**A'',B''**) and in (**C'',D''**) of the regions boxed in (**A',B')** and (**C',D')**, respectively, show no differences in the distribution of the polarity markers in the three epithelia of the *trol* mutant (*trol*$^{JO271\#49}$). Scale bar (20 μm) is indicated in (**A')** for complete sections and in (**A'')** for close-ups. The squamous epithelium and the apical side of the columnar cells are to the left, and dorsal is up.

Figure S3: **Both autonomous and non-autonomous sources of Trol contribute to the overall architecture of the wing disc**

(**A-D'**) Confocal longitudinal sections parallel to the dorsal/ventral axis (**A-D**, plane of section shown by the white dashed line in **A'**) and confocal images of xyz section of the squamous epithelium (**A'-D'**) of late third instar wing discs of the indicated genotype, labeled by immunofluorescence for Trol (green), stained with DAPI to highlight nuclei (red, or white when shown alone) and with phalloidin to reveal F-actin (blue, or white when shown alone). (**A-D**) The squamous epithelium is to the left and dorsal is up. (**A'-D'**) Anterior is to the right and dorsal is up. Scale bars (20 μm) for xzy sections are shown on the separate channel for F-actin in (**A**), and for xyz sections, on the separate channel for DAPI in (**A''**).

(**A-D'**) Autonomous or non-autonomous depletion of the wing disc BM Trol at 29°C using *UAS-trol.RNAi*^{JF03376} and *UAS-Dcr-2* with *C-765GAL4 (C765)* or *PplGAL4* (*Ppl*), respectively, does not have much of a consequence on the columnar epithelium and the folding of the cuboidal epithelium of the ventral pleura (**A,B,C,** folds numbered 1 to 4), or on the morphology of the squamous epithelium as seen by the distance between its cell nuclei (**A',B',C'**, region encompassed by the double-sided arrows). We note nonetheless that with *PplG4*, nuclei are closer to one another than in the control (compare **C'** to **A'**). *trol* depletion with both *GAL4*, however, induces a compression of the cuboidal epithelium of the ventral pleura (**D**, particularly visible for the fold number 2) and causes a packing of most of the nuclei at the level of the squamous epithelium (**D'**).

(**E**) Quantification of the width of the squamous epithelium along the double-sided arrows shown in (**A'-D'**). The dataset is represented by box-and-whisker plots. Horizontal lines are medians and box hinges are 25th and 75th percentiles. Whiskers indicate 5th and 95th percentiles and the black dot is a value beyond these limits. Pairwise comparisons with the Wilcoxon rank sum test and Benjamini-Hochberg correction were used (***: $p<0.001$, **: $p<0.01$). *wt*: N=10, *C765*: N=10, *Ppl*: N=9, *C765 Ppl*: N=7. Non-parametric statistics and plots were obtained with the R software.

Figure S4: **The reduction in the surface area of the SE's cells of the *trol* mutant is not due to ectopic cell death or impaired proliferation**

(**A,B**) Confocal images of late third instar wing discs of the indicated genotype, labeled by immunofluorescence for activated Caspase 3 (Casp, green, or white when shown alone) (**A**), or phosphorylated histone H3 (pH3, blue, or white when shown alone) (**B**). Scale bars (20 μm) for (**A**) and (**B**) are, respectively, indicated on the separate channel for Casp and pH3 on the image of the wild-type (*wt*) squamous epithelium (SE). Anterior is to the right and dorsal is up.

(**A**) Dead cells are not visible in any of the epithelia of the *wt* or the *trol* mutant (*trol*$^{JO271\#49}$) wing discs.

(**B**) The SE is labeled by the expression of a cytoplasmic GFP (green) under the control of *AGiRGAL4*. Proliferating cells are not detected in the SE of either the *wt* or the *trol* mutant (*trol*$^{JO271\#49}$, arrows point to pH3 positive nuclei -that appear as pink- outside of the SE), whereas they are present in the columnar epithelium (CoE) of both samples.

Figure S5: The wing disc displays three BMs with different ultrastructure and specific to the epithelium they underlie

(**A**) Bright-field picture of a late third instar wing disc illustrating the plane of section (white dotted bar) of confocal images (**B,B'**) or TEM micrographs (**C**, ultra-thin section, picture **1** to **7** ultra-thin sections taken at the same magnification, close-ups corresponding to the regions boxed and numbered in **C**). (**A,C**) the green line indicates the approximate anterior/posterior boundary and the asterisk in (**C**) points to a tear in the tissue. Scale bar for the TEM semi-thin section (50 μm) is indicated on the micrograph (**C**), and scale bar for the TEM ultra-thin sections (1 μm) is indicated on picture **1**.

(**B,B'**) in a wild-type wing disc, Trol protein (red, shown alone in **B'**) is present on the basal side of cells (SE: squamous epithelium, CoE: columnar epithelium) and accumulates in two regions underneath the folds of the wing pouch (white arrows).

(**1-7**) The BM (yellow brackets) changes morphology as the epithelium converts from a squamous to cuboidal shape and then from a cuboidal to columnar shape. The BM of the SE is thin and dense (picture **1**). As the epithelium changes shape, the BM remains dense but starts to thicken in the region where cells are cuboidal (picture **2**). When the epithelium adopts its columnar shape, the BM begins to show a layered structure (picture **3**) which becomes obvious in picture **4**. Thereafter, the BM exhibits electron-lucent parts with dots in between the layers forming a network (picture **5**). It reaches its maximum height at the fold of the wing pouch (picture **6** and arrow in **c**) and maintains its organization with a slight decrease in height underneath the center of the pouch (picture **7**). The maximum height of the BM roughly corresponds to regions of Trol accumulation (**B,B'**). Asterisks in picture **6** point to basal feet processes that are cross-sectioned.

Note that this sample is the control shown in Fig 3A.

Figure S6: **Decreasing Col IV in the *trol* mutant reduces the surface area and the major elongation axis defects of the SE's cells**

(**A-D**) Maximum-intensity projections of Dlg staining of wing discs of the indicated genotype were used to segment all the cells of the squamous epithelium (SE) with Epitools. (**A,B**) The black square for the wild-type (*wt*), and the black outline for the *trol* mutant ($trol^{JO271\#49}$) or the *trol* mutant with one copy of a mutant allele for *Viking* ($Vkg^{+/-}$), indicate the region where the cell surface area was plotted in (**A',B'**). For all discs, anterior is to the right and dorsal is up.

(**A',B'**) Datasets are represented by bee swarm plots. Horizontal lines are medians and whiskers are 25th and 75th percentiles. Each dot represents the value for an individual cell. (**A'**) *wt*: N=492 cells from 13 wing discs, *JO271#49*: N=888 cells from 14 wing discs. (**B'**) *JO271#49*: N=264 cells from 5 wing discs, *JO271#49* $Vkg^{+/-}$: N=213 cells from 4 wing discs. Non-parametric statistics and plots were obtained with the GraphPad Prism software. Data were subjected to the Wilcoxon rank sum test and show a strong decrease in the planar surface area of the SE's cells in absence of Trol (**A'**), which is significantly rescued upon introduction of one copy of a mutant allele for *Viking* ($Vkg^{+/-}$) in the genetic background (**B'**). ****: $p<0.0001$.

(**C,D**) The cell skeletons resulting from the segmentation are represented in red with the major elongation axis of the cell in green. This axis switches from isotropic to anisotropic in the *trol* mutant (**C**), and the isotropy is restored by the decrease in Col IV (**D**). Scale bar (20 μm) is shown on the wild-type for (**C**), and on the *trol* mutant for (**D**).

Figure S1

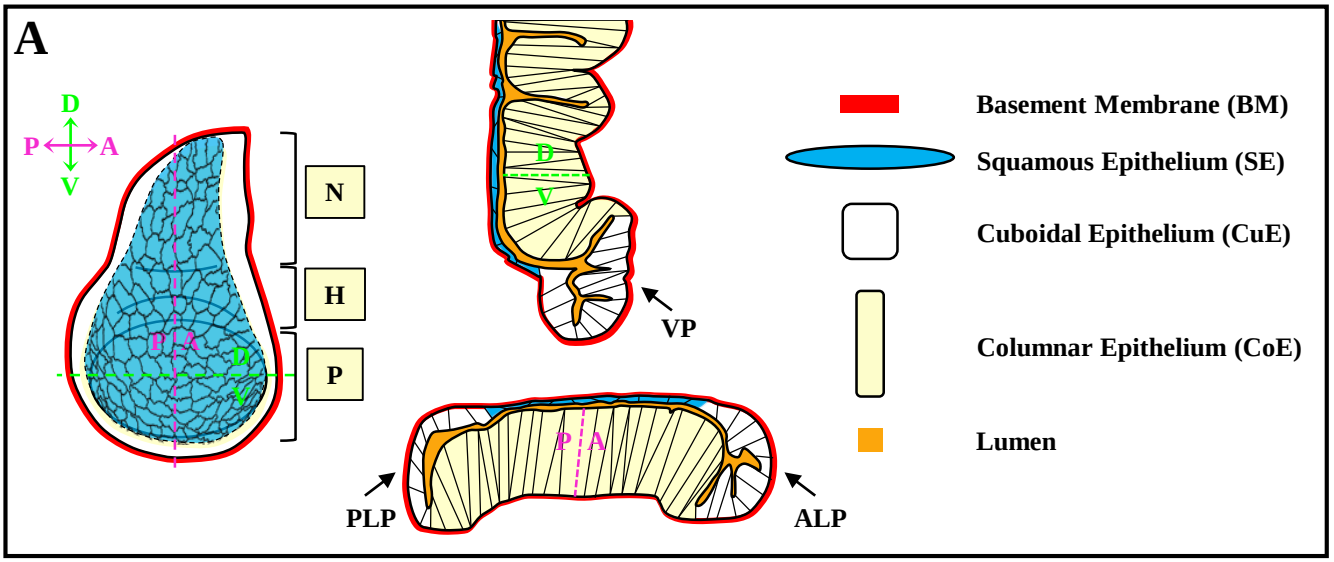
A
D
P
A
V
N
H
P
D
V
P
A
D
V
VP
PLP
ALP
Basement Membrane (BM)
Squamous Epithelium (SE)
Cuboidal Epithelium (CuE)
Columnar Epithelium (CoE)
Lumen

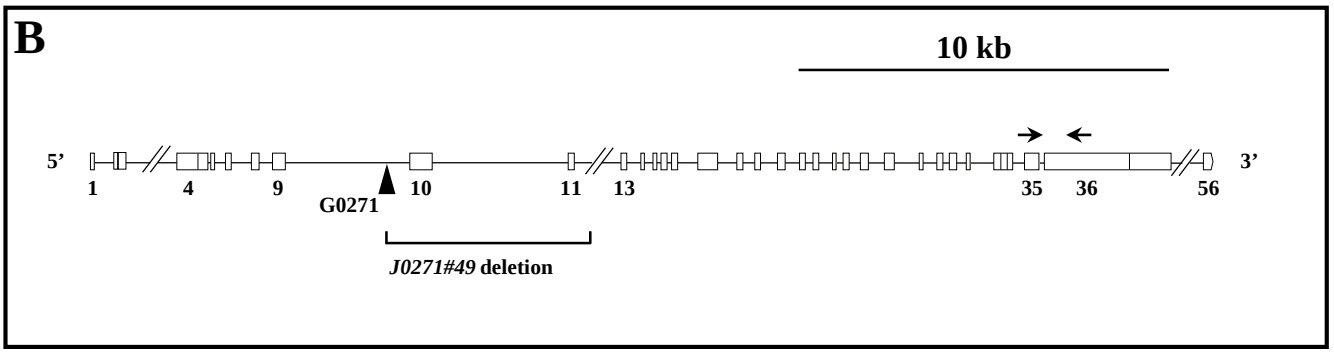
B
10 kb
5'
3'
1
4
9
G0271
10
11
13
35
36
56
J0271#49 deletion

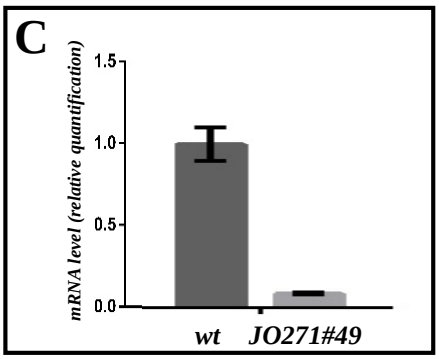
C
mRNA level (relative quantification)
1.5
1.0
0.5
0.0
wt
JO271#49

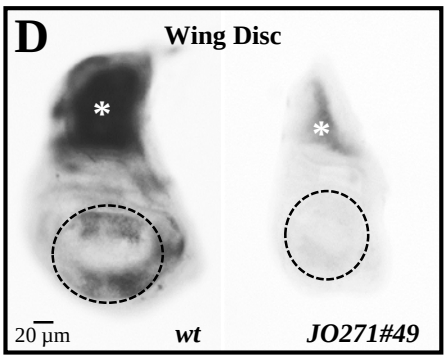
D
Wing Disc
20 µm
wt
JO271#49

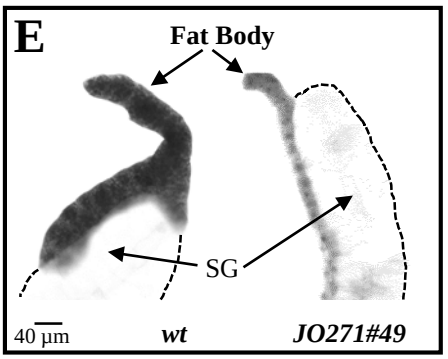
E
Fat Body
SG
40 µm
wt
JO271#49

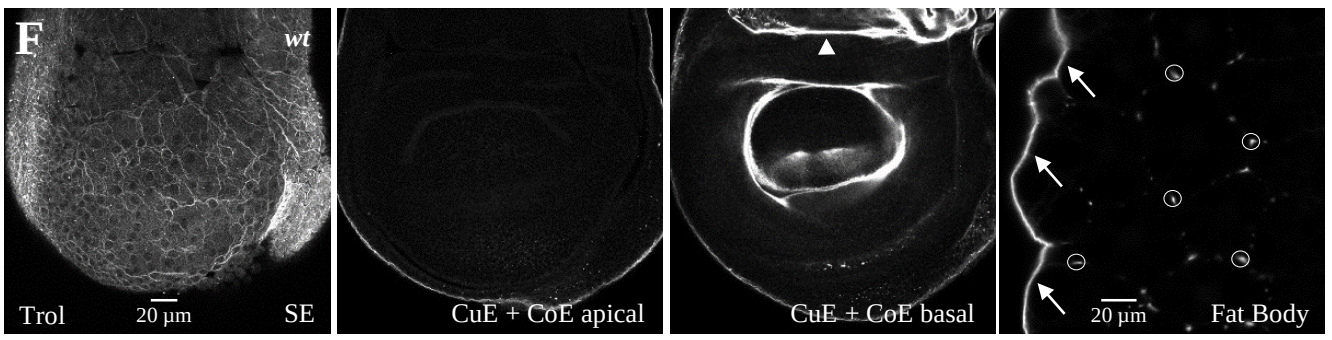
F
wt
Trol
20 µm
SE
CuE + CoE apical
CuE + CoE basal
20 µm
Fat Body

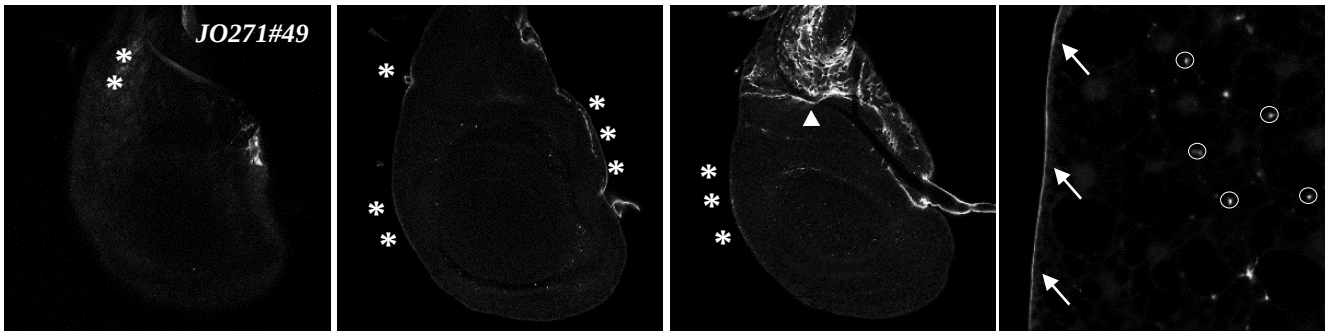
JO271#49

Figure S2

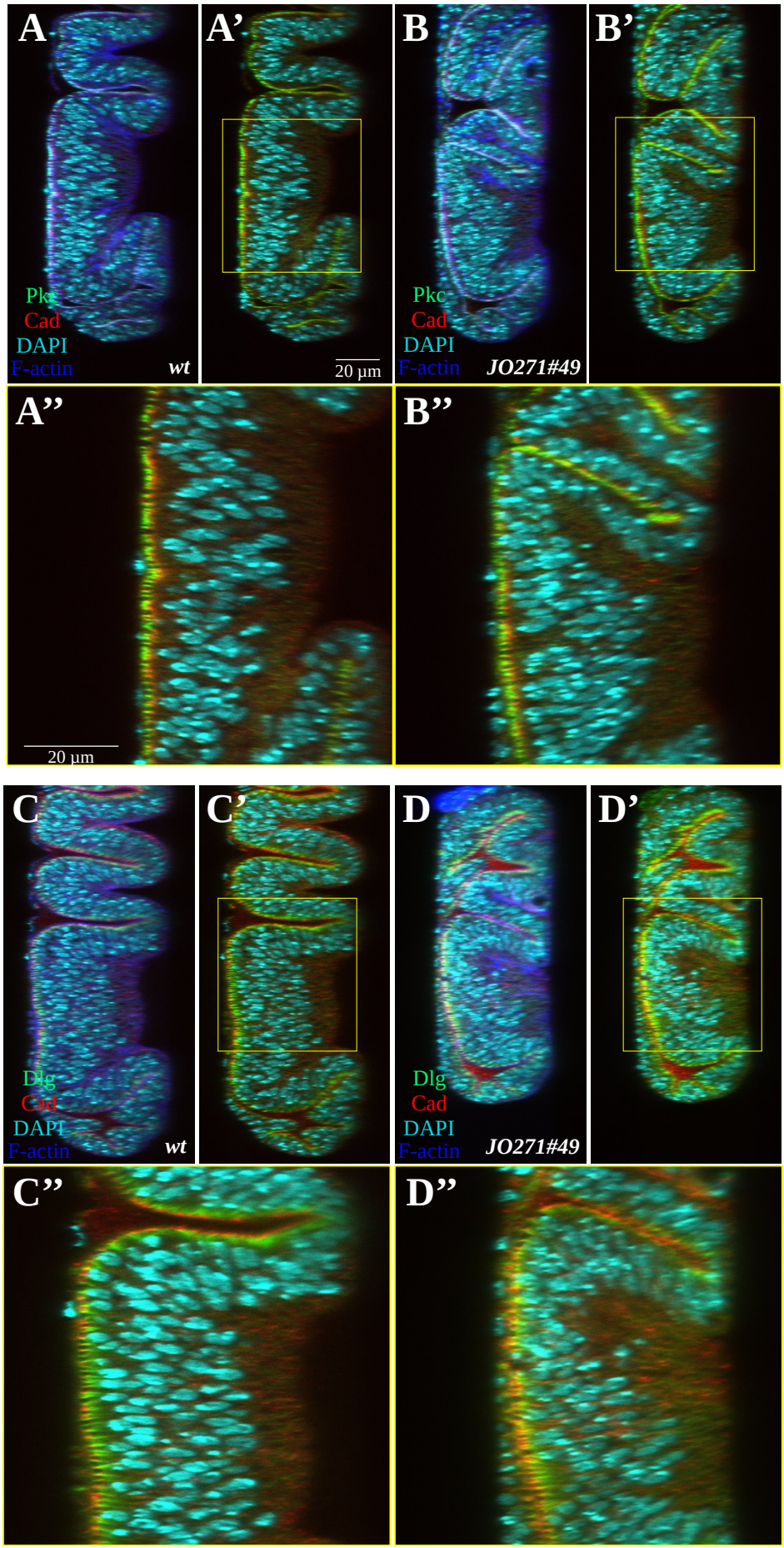
A
A'
B
B'
Pkc
Cad
DAPI
F-actin
wt
20 µm
JO271#49
A''
B''
20 µm
C
C'
D
D'
Dlg
Cad
DAPI
F-actin
wt
JO271#49
C''
D''

Figure 1

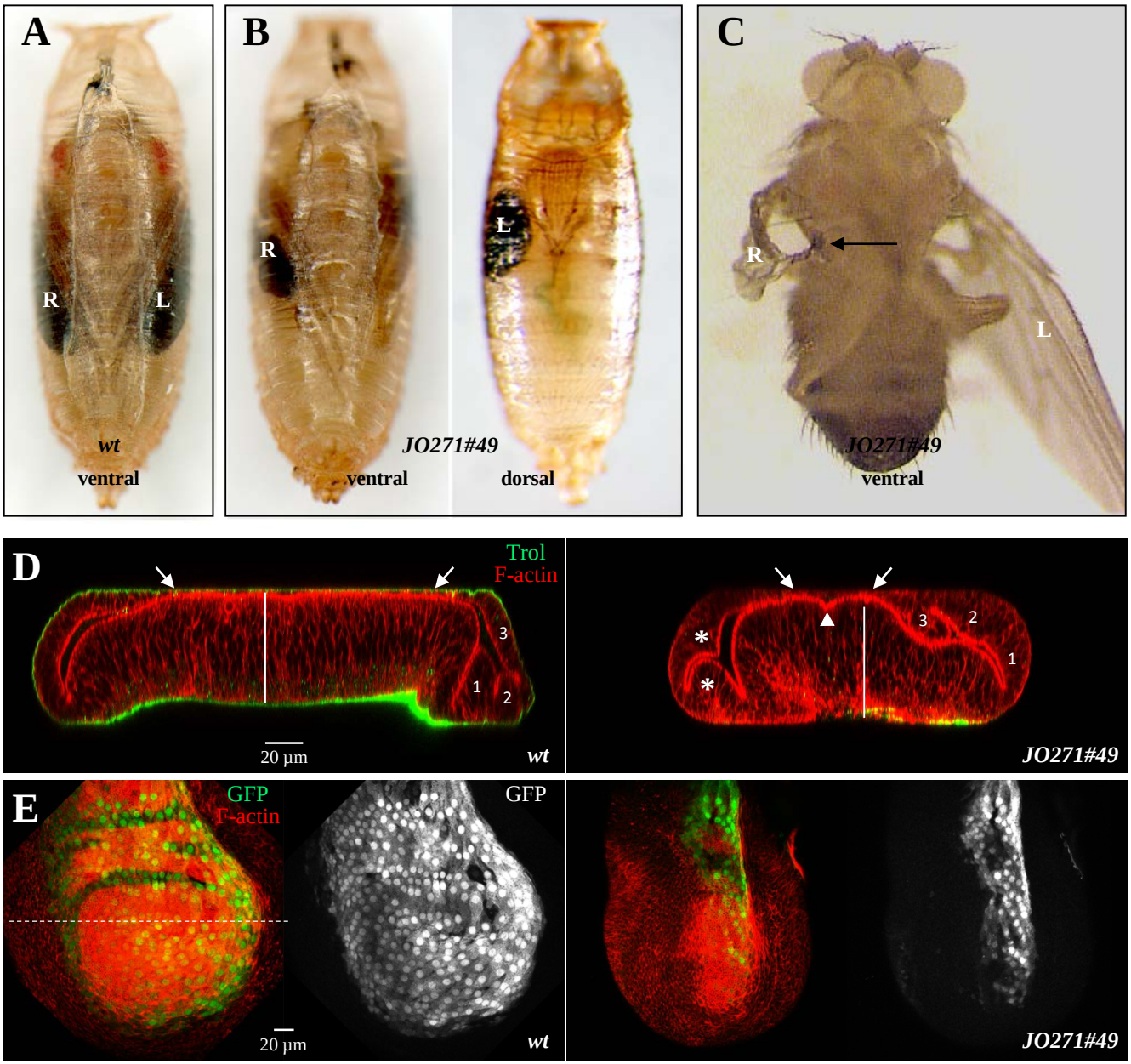
A
R
L
wt
ventral
B
R
L
JO271#49
ventral
dorsal
C
R
L
JO271#49
ventral
D
Trol
F-actin
3
1
2
20 µm
wt
3
2
1
JO271#49
E
GFP
F-actin
20 µm
wt
GFP
JO271#49

Figure S3

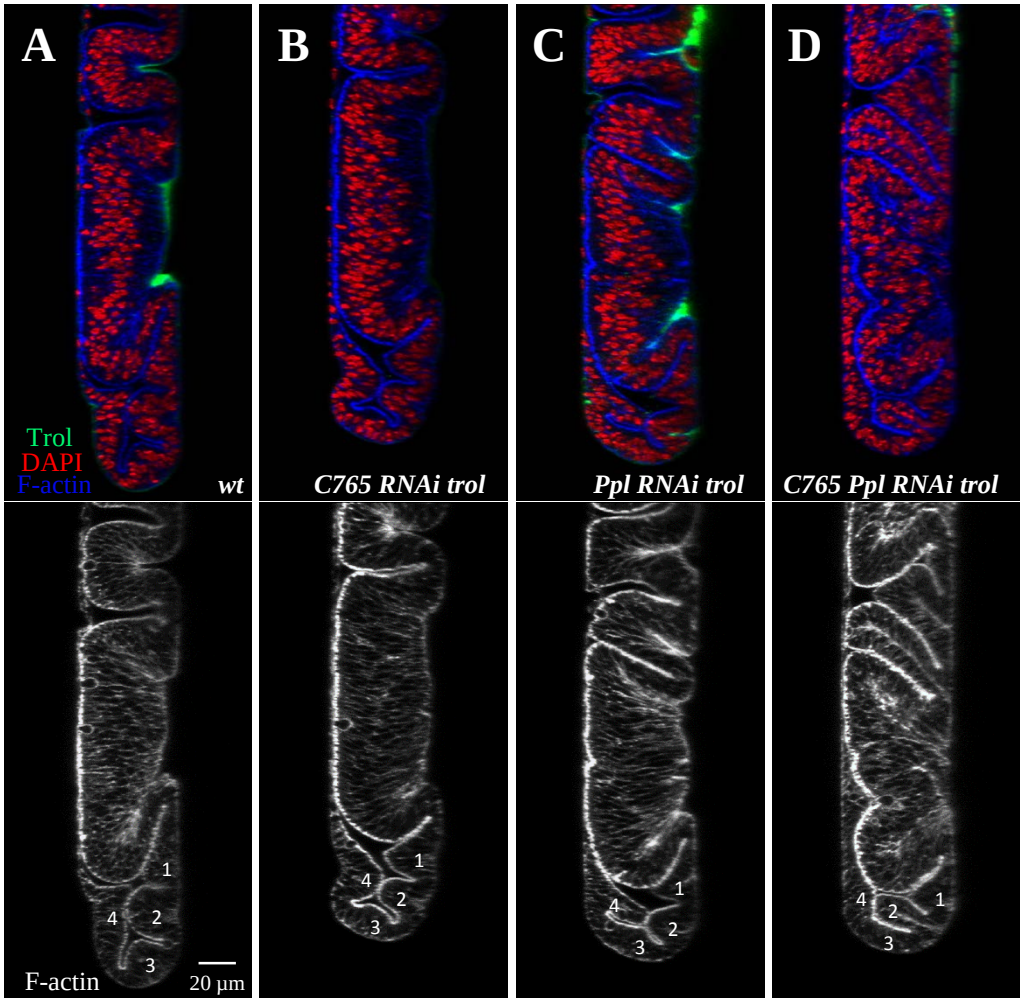
A
B
C
D
Trol
DAPI
F-actin
wt
C765 RNAi trol
Ppl RNAi trol
C765 Ppl RNAi trol
1
2
3
4
F-actin
20 µm

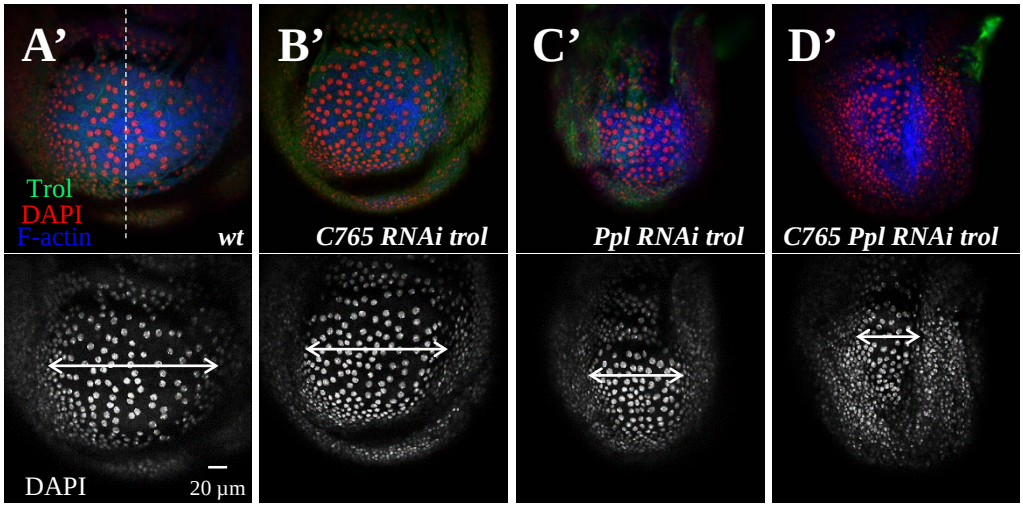
A'
B'
C'
D'
Trol
DAPI
F-actin
wt
C765 RNAi trol
Ppl RNAi trol
C765 Ppl RNAi trol
DAPI
20 µm

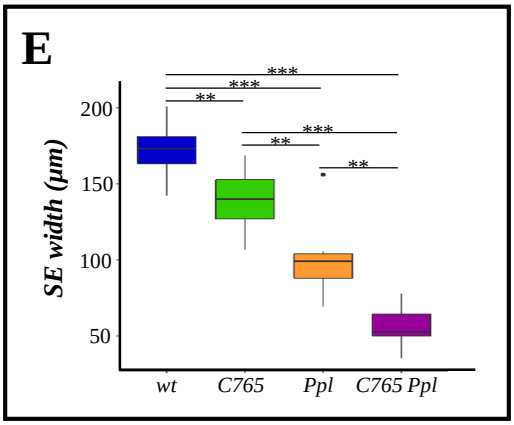
E
SE width (µm)
200
150
100
50
***
***
**
***
**
**
wt
C765
Ppl
C765 Ppl

Figure S4

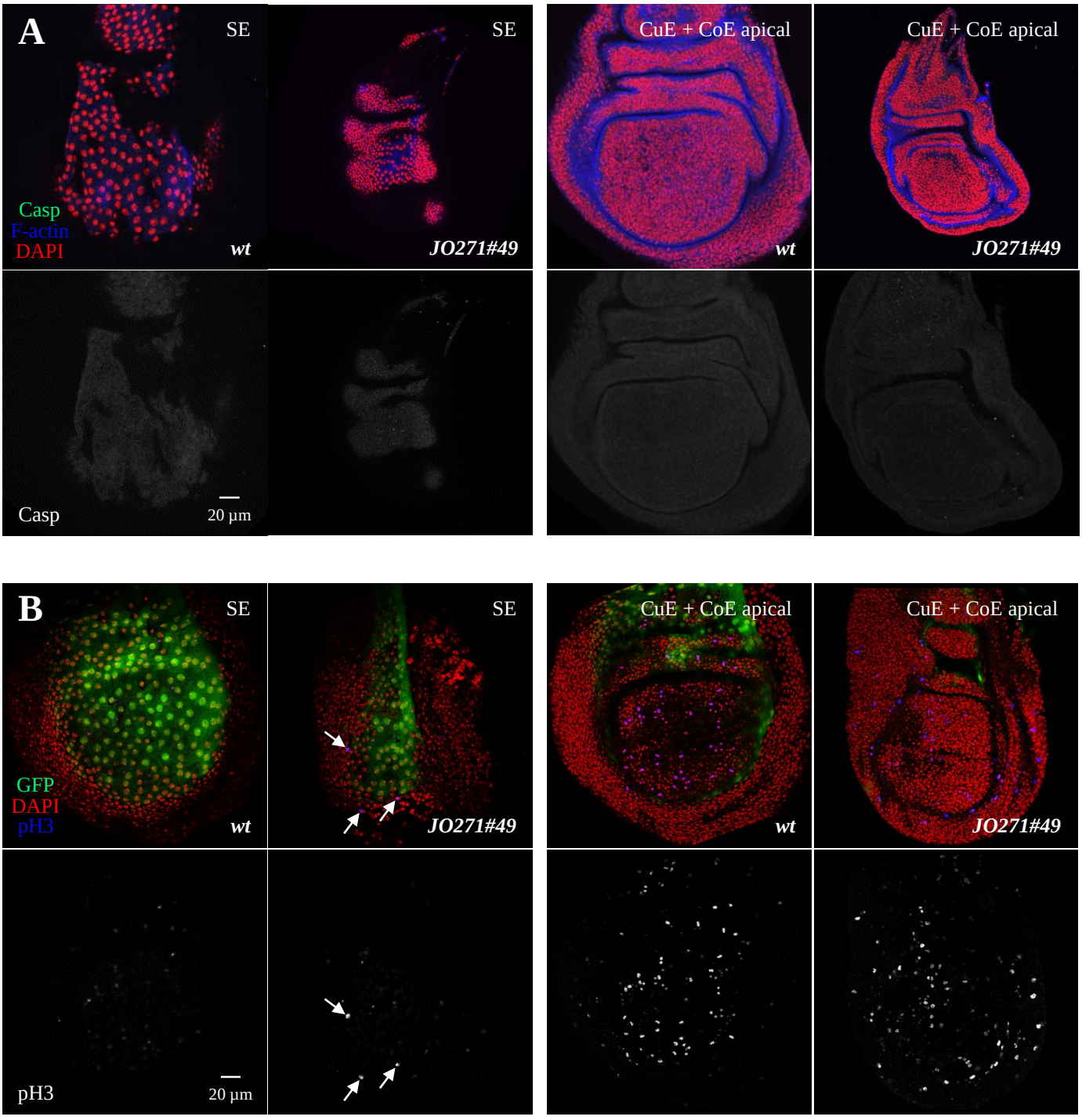
A
SE
SE
CuE + CoE apical
CuE + CoE apical
Casp
F-actin
DAPI
wt
JO271#49
wt
JO271#49
Casp
20 µm
B
SE
SE
CuE + CoE apical
CuE + CoE apical
GFP
DAPI
pH3
wt
JO271#49
wt
JO271#49
pH3
20 µm

Figure 2

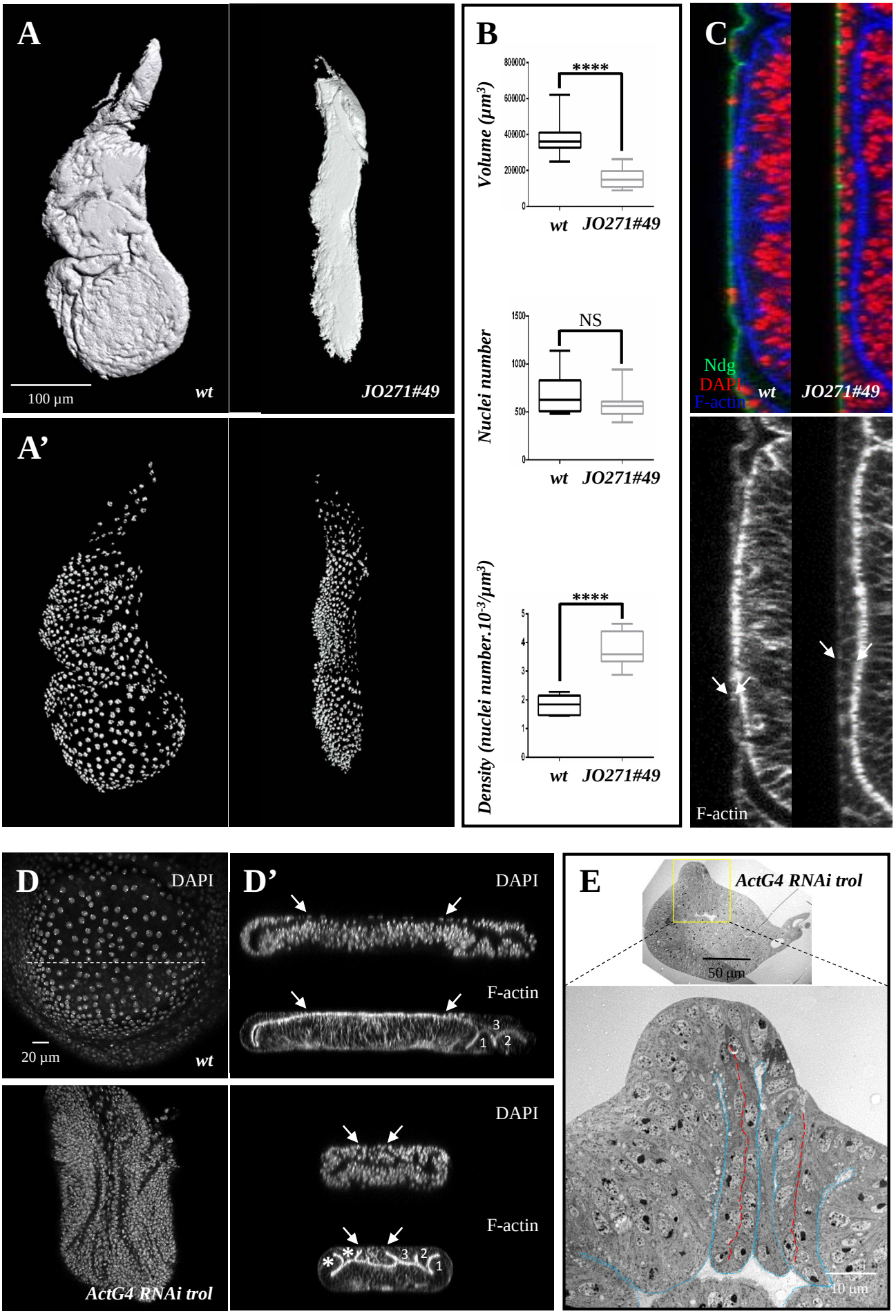
A
100 µm
wt
JO271#49
A'
B
Volume (µm3)
800000
600000
400000
200000
0
****
wt
JO271#49
Nuclei number
1500
1000
500
0
NS
wt
JO271#49
Density (nuclei number.10-3/µm3)
5
4
3
2
1
0
****
wt
JO271#49
C
Ndg
DAPI
F-actin
wt
JO271#49
F-actin
D
DAPI
20 µm
wt
D'
DAPI
F-actin
1
2
3
ActG4 RNAi trol
DAPI
F-actin
1
2
3
*
*
E
ActG4 RNAi trol
50 µm
10 µm

Figure 3

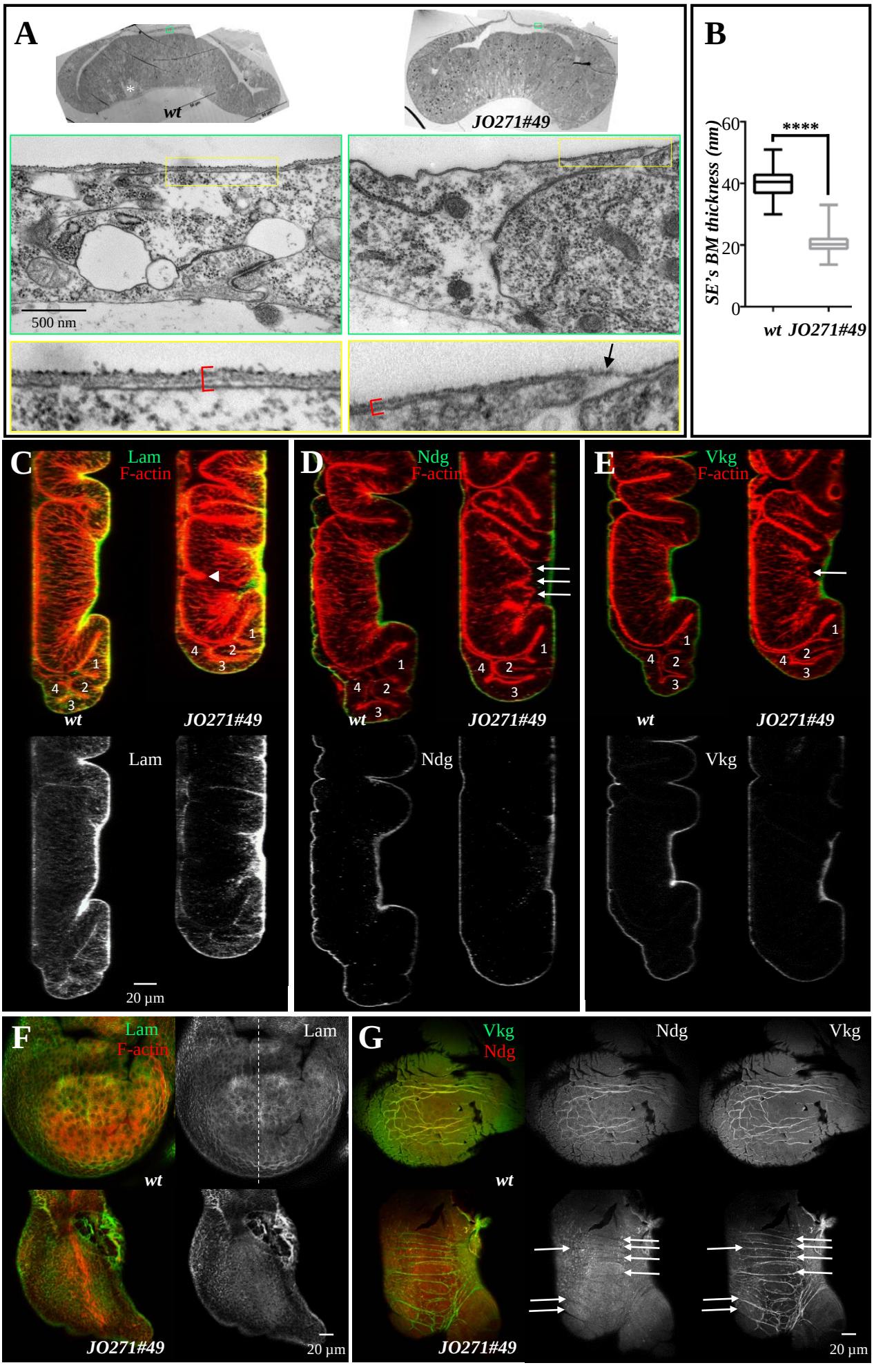
A
wt
JO271#49
500 nm
B
SE's BM thickness (nm)
60
40
20
0
****
wt
JO271#49
C
Lam
F-actin
wt
JO271#49
Lam
20 µm
D
Ndg
F-actin
wt
JO271#49
Ndg
E
Vkg
F-actin
wt
JO271#49
Vkg
F
Lam
F-actin
Lam
wt
JO271#49
20 µm
G
Vkg
Ndg
Ndg
Vkg
wt
JO271#49
20 µm

Figure S5

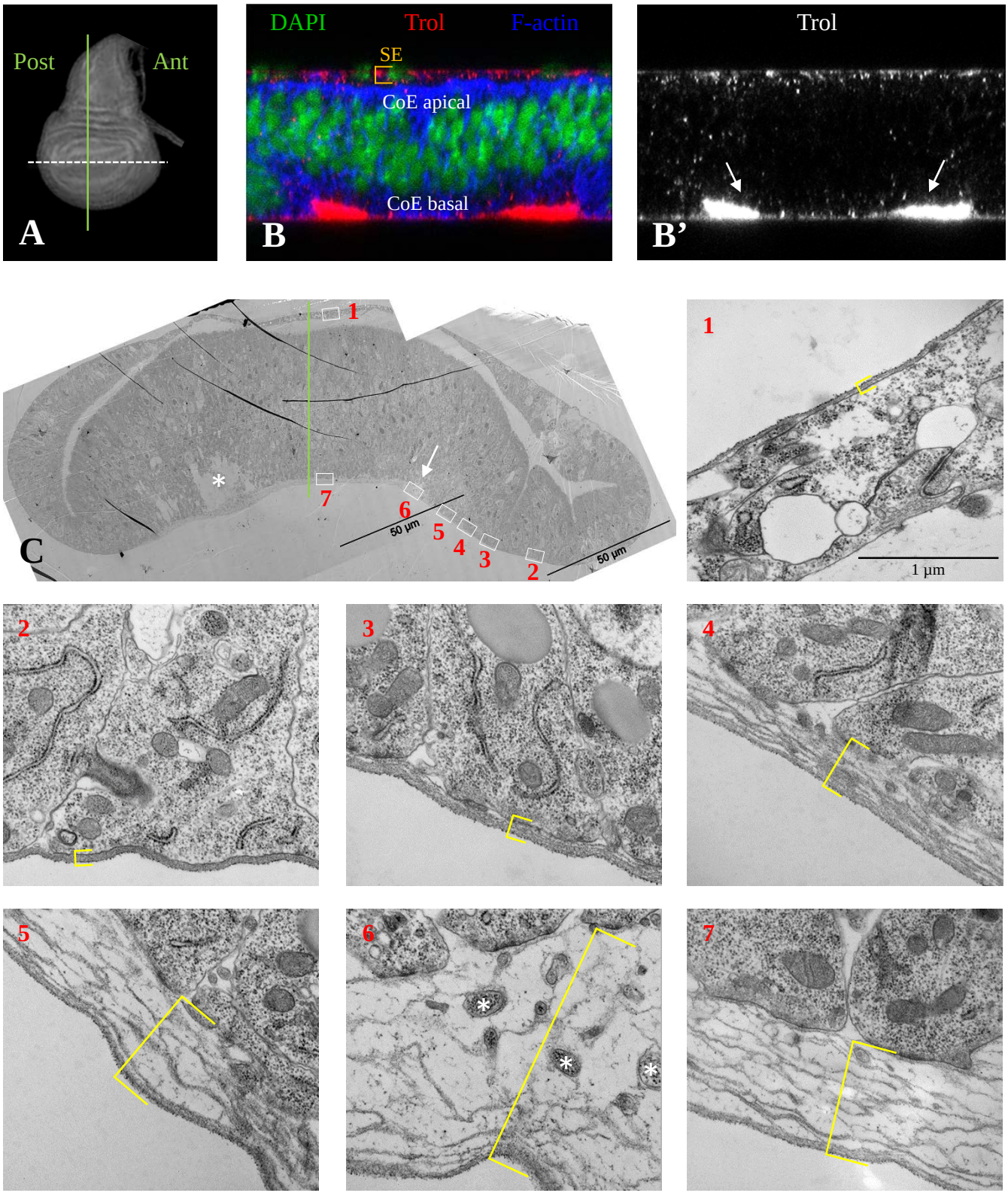
Post
Ant
A
DAPI
Trol
F-actin
SE
CoE apical
CoE basal
B
Trol
B'
C
1
7
6
5
4
3
2
50 µm
50 µm
*
1
1 µm
2
3
4
5
6
7
*
*
*

Figure S6

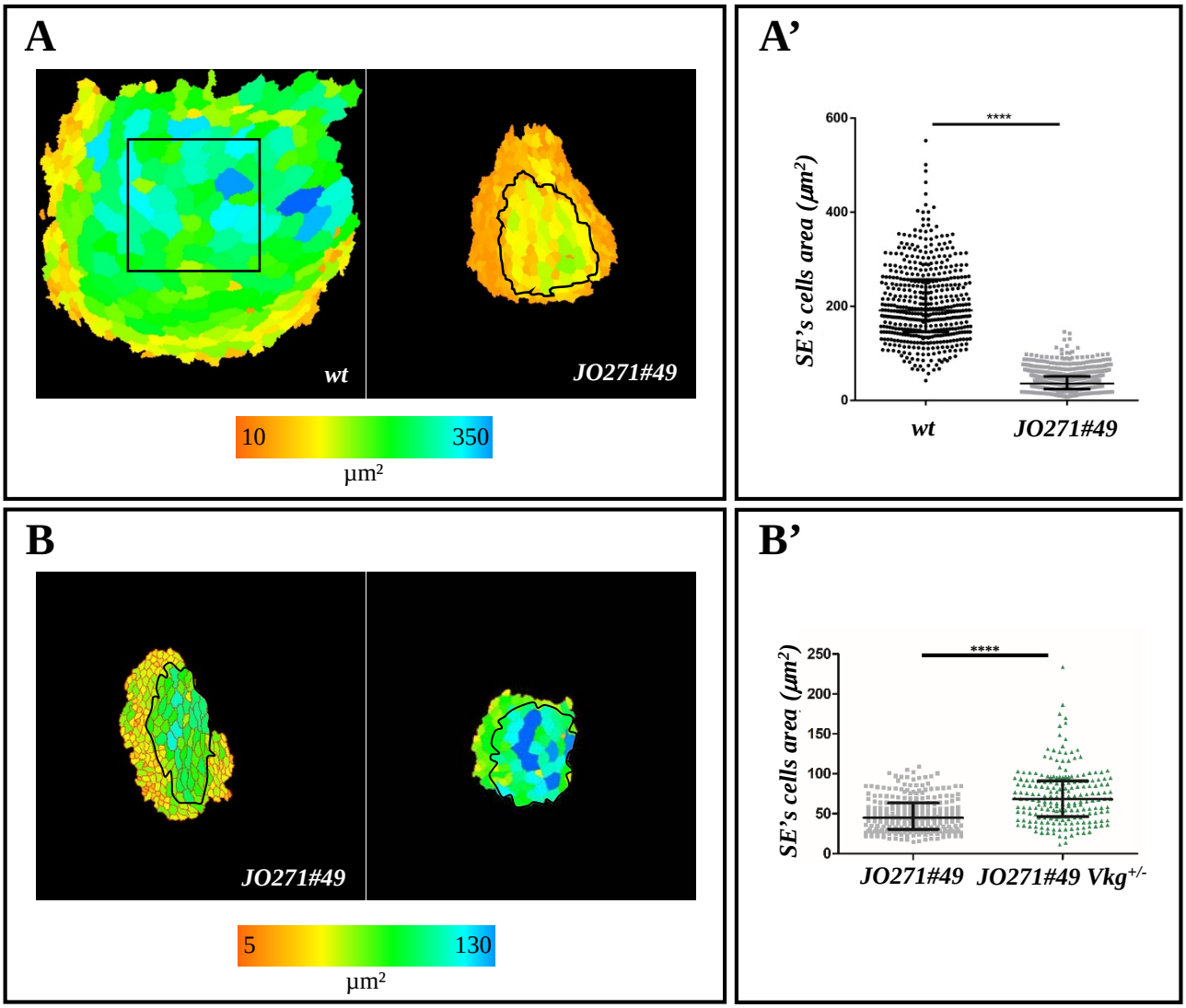
A
wt
JO271#49
10
350
µm²
A'
SE's cells area (µm²)
600
400
200
0
****
wt
JO271#49
B
JO271#49
5
130
µm²
B'
SE's cells area (µm²)
250
200
150
100
50
0
****
JO271#49
JO271#49 Vkg+/-
C
20 µm
wt
JO271#49
D
20 µm
JO271#49
JO271#49 Vkg+/-

Figure 4

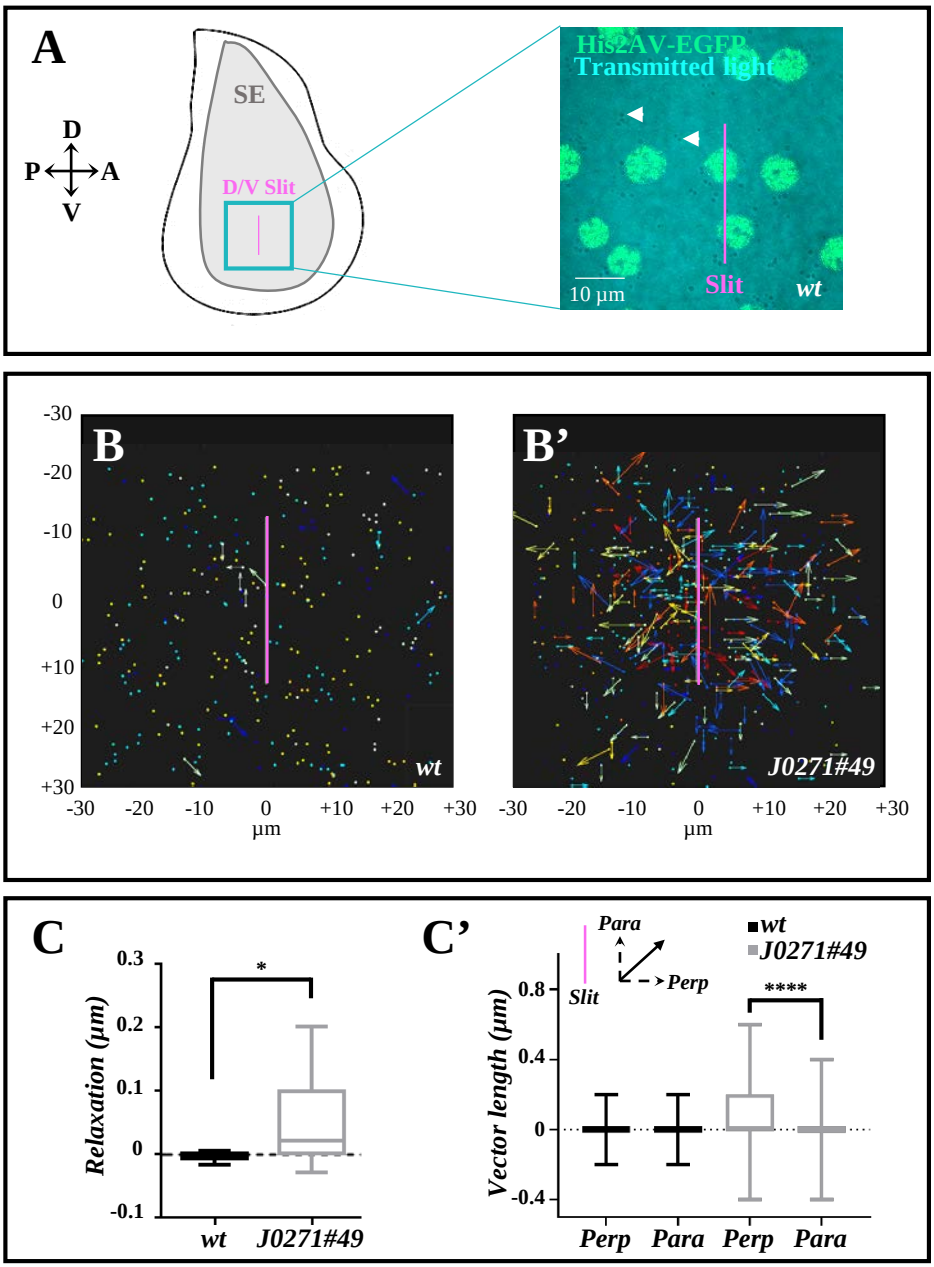
A
D
P
A
V
SE
D/V Slit
His2AV-EGFP
Transmitted light
10 µm
Slit
wt
B
B'
wt
J0271#49
-30
-20
-10
0
+10
+20
+30
µm
C
C'
Relaxation (µm)
0.3
0.2
0.1
0
-0.1
*
wt
J0271#49
Para
Perp
Slit
wt
J0271#49
Vector length (µm)
0.8
0.4
0
-0.4
****
Perp
Para
Perp
Para

Figure 5

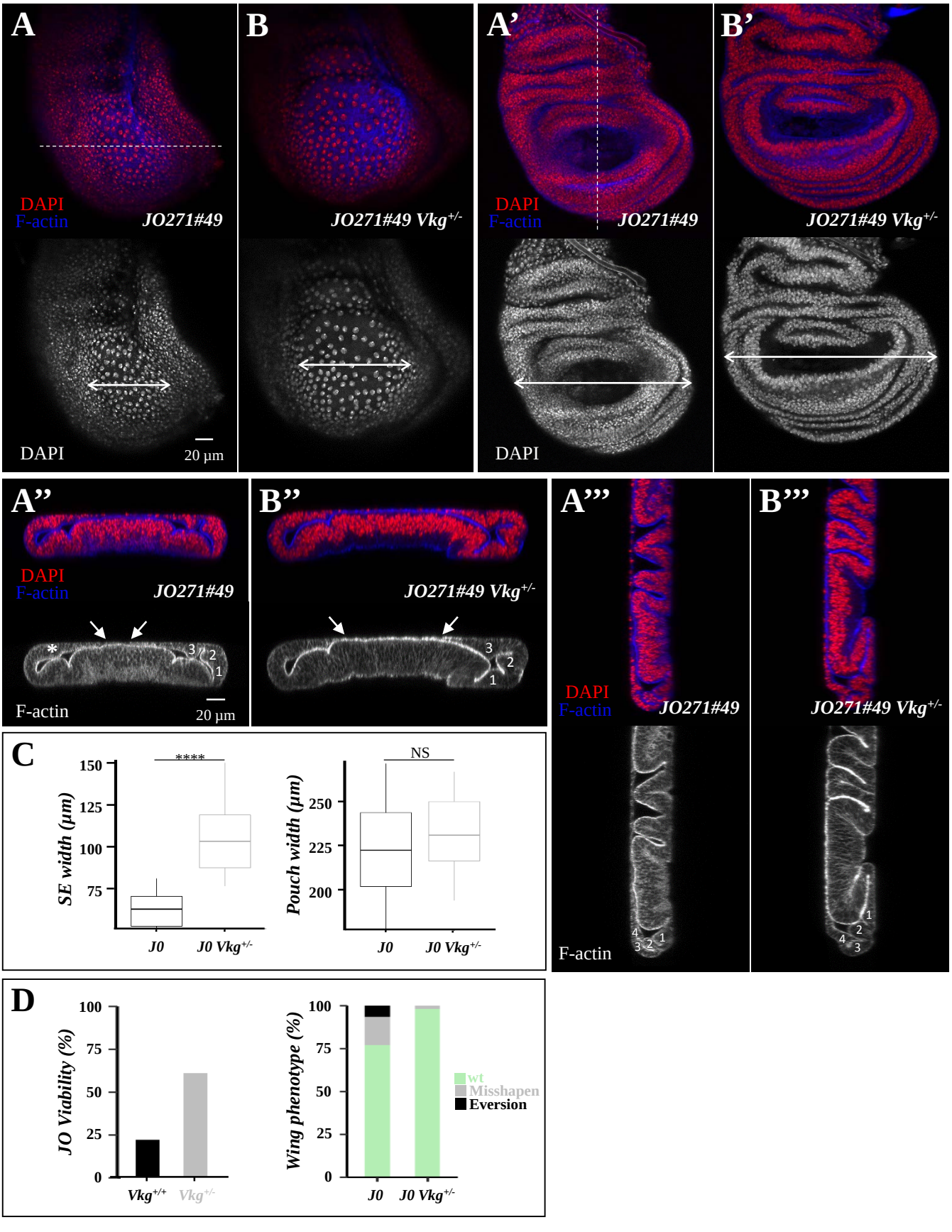
A
B
A'
B'
DAPI
F-actin
JO271#49
JO271#49 Vkg+/-
DAPI
20 µm
A''
B''
F-actin
A'''
B'''
C
SE width (µm)
Pouch width (µm)
****
NS
J0
J0 Vkg+/-
D
JO Viability (%)
Vkg+/+
Vkg+/-
Wing phenotype (%)
wt
Misshapen
Eversion

Figure 6

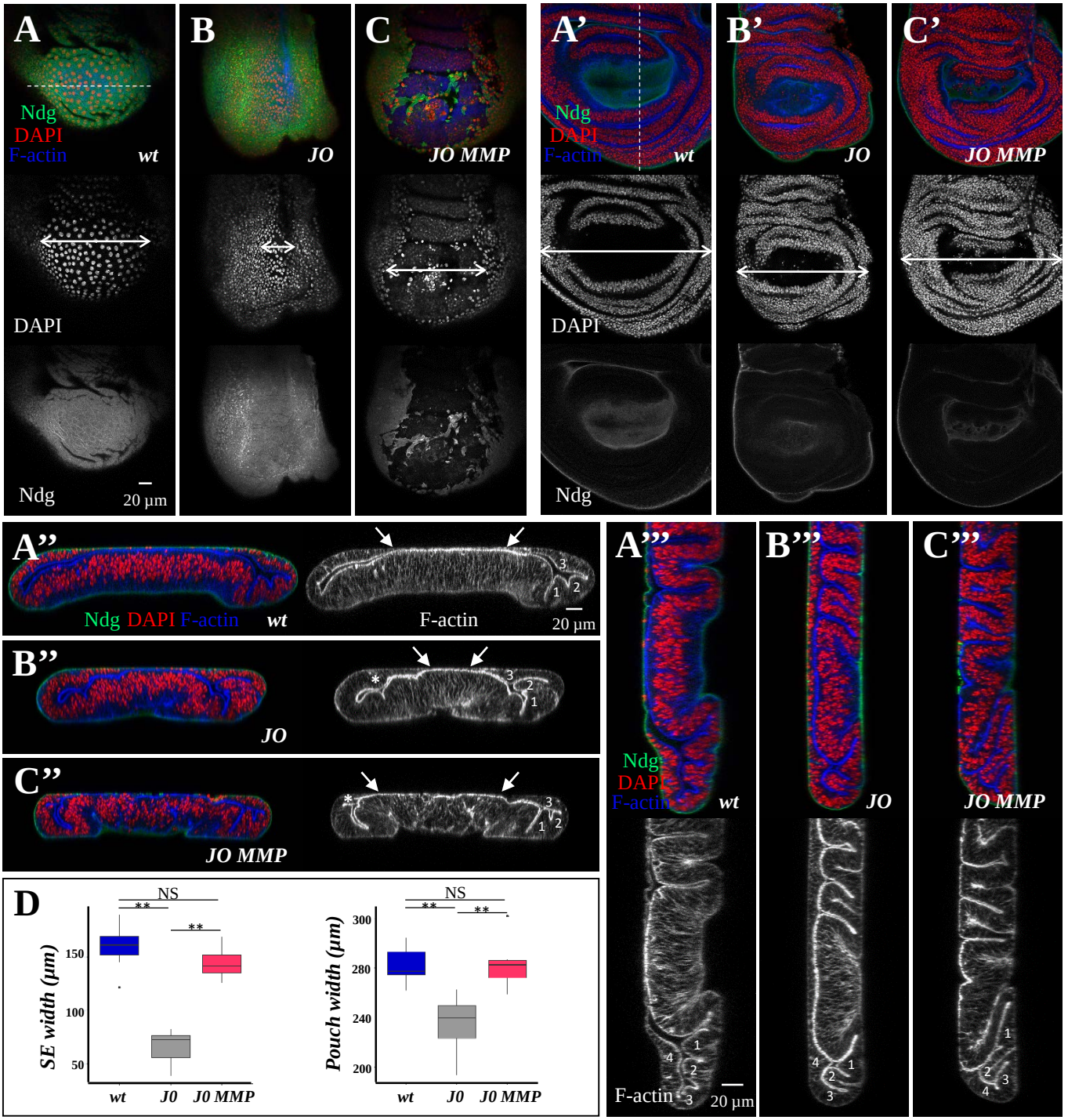
A
B
C
A'
B'
C'
Ndg
DAPI
F-actin
wt
JO
JO MMP
DAPI
Ndg
20 µm
A''
B''
C''
Ndg DAPI F-actin
F-actin
A'''
B'''
C'''
D
SE width (µm)
Pouch width (µm)
NS
**
wt
J0
J0 MMP